CHARACTERIZATION OF AERODYNAMIC AND AEROACOUSTIC PERFORMANCE OF BLADELESS FANS

A Thesis

Submitted to the Faculty

of

Purdue University

by

Ang Li

In Partial Fulfillment of the

Requirements for the Degree

of

Master of Science

August 2019

Purdue University

West Lafayette, Indiana

THE PURDUE UNIVERSITY GRADUATE SCHOOL
STATEMENT OF THESIS APPROVAL

Dr. Jun Chen, Co-chair

School of Mechanical Engineering

Dr. Tom Shih, Co-chair

School of Aeronautics and Astronautics Engineering

Dr. Gregory Blaisdell

School of Aeronautics and Astronautics Engineering

Approved by:

Dr. Weinong Wayne Chen

Head of the School Graduate Program

ACKNOWLEDGMENTS

Foremost, I would like to express my sincere gratitude to my advisor Professor Chen for the continual support of my research, for his patience, motivation, enthusiasm, and immense knowledge. His guidance helped me in all the time of research. I am especially thankful for his patience and meticulous feedback on my writing.

I would also like to thank the members of my committee: Prof. Shih and Prof. Blaisdell, for their suggestions on the courses and my research.

I would also like to thank the experts who were involved in this research project: Prof. Bolton, Prof. Davies and Prof. Liu. Without their guidance and help, the aeroacoustic analysis could not have been successfully conducted.

I would also like to thank the Midea Global Innovation Center for sponsoring my studies. I am also grateful for their technical and professional guidance and feedback on my research.

I would also like to acknowledge School of Aeronautics and Astronautics Engineering and School of Mechanical Engineering at Purdue University for being such good teachers of my work and life.

I would also like to thanks for the support and care from my colleagues.

Finally, I must express my very profound gratitude to my parents for providing me with persistent support and continuous encouragement throughout my years of study. This accomplishment would not have been possible without them. Thank you.

TABLE OF CONTENTS

Page

LIST OF TABLES

LIST OF FIGURES

ABBREVIATIONS

CFD	computational fluid dynamics
CAA	computational aeroacoustic
FW-H	Ffowcs Williams and Hawkings analogy
LES	Large Eddy Simulation
RANS	Reynolds-Averaged Navier-Stokes turbulence model
SPL	sound pressure level

NOMENCLATURE

c	Chord length of the wind channel cross-section
d	Slit width of the wind channel
D	Length scale of the intake
f	Frequency
H	Cross-sectional height of the wind channel
M_1	The ratio of Q_{total} and Q_{inlet}
M_2	The ratio of Q_{back} and Q_{inlet}
p	Sound pressure
p_{inlet}	Static pressure at the wind channel intake
p_{ref}	Reference pressure, 20μPa
Q_{back}	Mass flow rate entrained from the back of the bladeless fan
$Q_{entrained}$	Total mass flow rate entrained from the back and the side of the bladeless fan
Q_{inlet}	Mass flow rate suctioned into the bladeless fan from the intake
Q_{side}	Mass flow rate entrained from the side of the bladeless fan
Q_{total}	Total mass flow rate at $x = 1.5$m away from the bladeless fan
r	Distance away from the center of the wind channel inlet
t	flow time in Large Eddy Simulation
u_x	Mean velocity along x direction
u_{inlet}	Mean velocity at the bladeless fan intake
x_0	Slit location of the wind channel
x	Cartesian coordinate parallel to the direction of the streamwise
y	Cartesian coordinate perpendicular to the direction of streamwise and towards the left of the bladeless fan

z	Cartesian coordinate perpendicular to the direction of streamwise and towards the top of the bladeless fan
μ	Dynamic viscosity of air
ρ	Density of air
ψ	Circumferential position of the receivers
ω	Rotating speed of the rotor

ABSTRACT

Ang Li Master of Science, Purdue University, August 2019. Characterization of Aerodynamic and Aeroacoustic Performance of Bladeless Fans. Major Professor: Jun Chen.

Bladeless fans are well known for their unique shape and efficient performance, which have a great impact on the fan industry. At present, there are few studies on the bladeless fan and the research on the improvement of fan design is a lack. Therefore, the study on the performance of the bladeless fan with different design is the main purpose of this thesis.

In the present study, a bladeless fan prototype is created and studied by numerical simulations. When characterizing the aerodynamic and aeroacoustic performances of the bladeless fan, the entire fan prototype, including wind channel, base, rotor and stator, is adopted; when investigating the influence of the wind channel's geometric parameters, only wind channel is considered in simulations. The influence of the slit width, the height of the cross-section, the slit location and the profile of the cross-section are studied.

It is found that the flow outside the bladeless fan consists of the air blown out from the wind channel and entrained from the back and side of the fan. The air entrained from the side is the main source of flow rate increase. As for the aeroacoustic performance, the rotor and stator inside the base are the predominated source of the noise generated by the bladeless fan.

The performances of the bladeless fan are very sensitive to the geometric details of the wind channel. The generated noise always increases as the wind strength improves. The slit width of the wind channel has the greatest impact. With the slit moves away from the leading edge, the wind produced by the bladeless fan becomes more powerful and the noise becomes louder. The cross-sectional height of 4cm has

the best aerodynamic performance but the generated noise is a little larger than other designs. The profile of the cross-section shows insignificant influence on the performances.

1. INTRODUCTION

1.1 Background

A fan is a powered machine used to generated flow within a fluid, especially in the air. Typically, air flows with high volume and low pressure are produced by the fan with rotating blades (Wallis, 2014). Nowadays, fans are widely used in industries. For example, fans are applied as the cooling system in the vehicle system and the CPU radiator. It is also widely used in HVAC (heating, ventilation, and air conditioning) system for ventilation (Cory, 2010). (Bruegmann, 1978). The most popular application is to cool people. They do not cool air significantly, but increase heat convection into the surrounding air due to the produced air flow (DOE, 2003).

The axial fan and centrifugal fan are two main types of fans used in industry (Boddy, 2001). The axial fan, as illustrated in Fig. 1.1(a), is a type of fan that leads air to flow through it in an axial direction which is parallel to the shaft about which the blades rotate. The flow is axial at both entry and exit. The fan produces a pressure difference, and then force is generated to cause a flow through the fan (Theodorsen, 1948). The centrifugal fan, as shown in Fig. 1.1(b), is a device for moving air in a direction at an angle to the incoming fluid, which usually includes a ducted housing to direct outgoing air in a specific direction (Cann and Duell, 1972). Centrifugal fans use the kinetic energy of the impellers to increase the volume of the air stream, which in turn moves against the resistance caused by ducts, dampers and other components. Centrifugal fans displace air radially, changing the direction of the airflow (Kind and Tobin, 1989).

Since the fans are widely used in industry, many research has been carried out in the past decades. Corsini et al. (Corsini et al., 2013) summarized the computational methods and application in industrial fan design. They elucidate how Reynolds-

(a) (b)

Figure 1.1. (a) Axial fan. (b) Centrifugal fan

averaged Navier-Stokes approach and large eddy simulation are applied to calculate the flow field of axial fans, centrifugal fans and ventilation systems. Meyer et al. (Meyer and Kröger, 2001) studied the flow field near an axial fan by numerical simulations. They model the axial flow fan as an actuator disc and uses blade element theory to calculate the actuator disc forces. It is found that the radial forces are small compared with the axial and tangential forces exerted on the fluid stream by the axial flow fan blades. The interaction noise radiated from an axial fan is calculated by Hu et al.(Hu et al., 2013). Their results show the scattering effect of the duct wall plays an important role in the prediction of rotorstator interaction noise and is able to increase the accuracy of the prediction. Reese et al.(Reese et al., 2007) predicted the aerodynamic noise source. Various computational methods, including LES, DES, SAS and URANS, are employed to predict the noise radiated by an axial fan. It is shown that LES is able to give the most accurate prediction. Jiang et al. (Jiang et al., 2007) investigate the aeroacoustic performance of the axial fan applied on a room air conditioner and illustrate the tip vortex affect the flow fields near the blade tip significantly and has a large blockage effect on the flow. Younsi et al. (Younsi et al., 2007), investigate the unsteady flow in the centrifugal fan by CFD and experiments. They found that the main source of flow perturbation and unsteadiness in a centrifugal fan is the volute tongue zone. The noise generated by the centrifugal fan is studied by Liu et al.(Liu et al., 2010). It is reported that the main source of tonal noise in the fan is the aerodynamic interactions between the impeller and the volute tongue.

Traditionally, fans are designed with visible blades and wind is produced by the rotating blades. In 2009, a new concept of fan, bladeless fan, was invented by James Dyson (Fitton et al., 2011). Compared to the traditional fan, the wind generated by the bladeless fan is softer and more uniform. Furthermore, since the bladeless fan has no visible blades, children will not be easily hurt by the rotating blades like in the traditional fans, the bladeless fan is much safer (Gammack et al., 2012). The bladeless fan uses the knowledge of jet engine and turbocharges technology of automotive for reference. It features compact structure and streamlined contour. Since the air velocity blown out from the outlet is very large, more air is entrained from upstream and side of the fan. Thus, compared to the traditional fan, the flow rate at downstream is much larger. The bladeless fan also promotes industrial development because of its innovative design. Many variations are invented, such as air purifiers, humidifiers and hair dryers.

Although bladeless fans have been widely acclaimed since its inception, they have some disadvantages. The noise generated by the bladeless fan is as high as that produced by traditional fans. In a high operating level, the noise produced by the high-speed jet from the outlet is sharp and harsh. In terms of the energy utilization efficiency, the resistance inside the wind channel of the bladeless fan is large, resulting to lower efficiency than that of the bladeless fan. In addition, the base structure of the bladeless fan is light and thin, so it may be stable and prone to reducing vibration.

1.1.1 Flow Characteristic of the Bladeless Fan

Figure 1.2 shows the typical air handling path of a typical bladeless fan, which is consisted of a base and a wind channel. The air intake is located at the base in which the motor, impeller and stator are set. An annular slit is located at the wind channel whose cross-section is of an airfoil profile. The air is sucked from the intake and driven into the wind channel by the enclosed motor-impeller combination. The air then exits the wind channel from the annular slit, forming a high-speed jet that induces a pressure gradient between the fan's front surface and its back surface. Due to the presence of this pressure gradient, the ambient air is entrained from the back and side of the fan, then moves forward, resulting in a significant increase of mass flow rate.

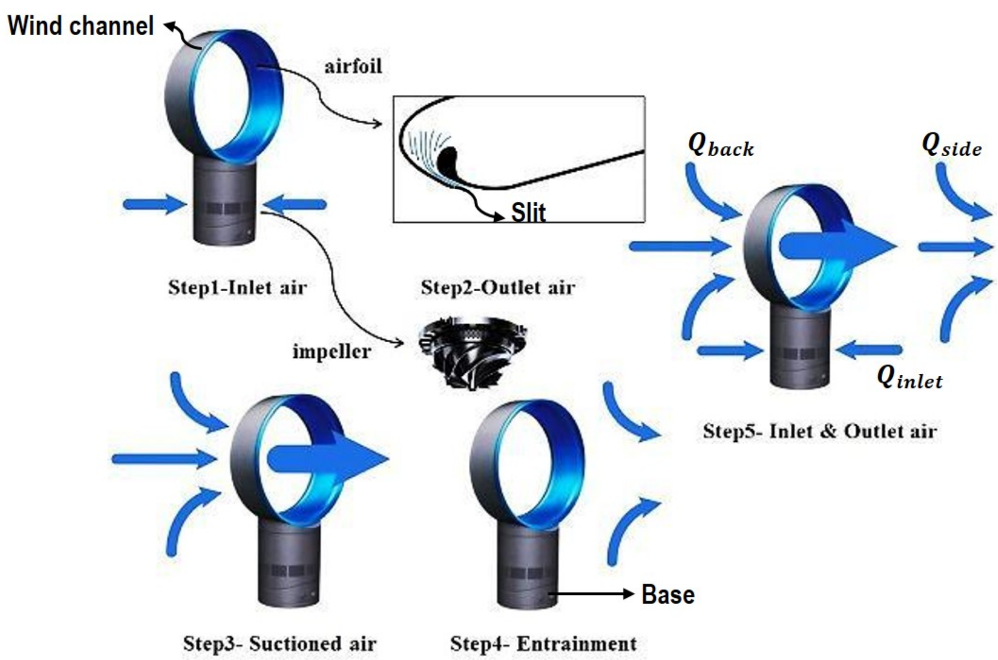

Figure 1.2. Air handling mechanism of the bladeless fan (Jafari et al., 2015)

The flow inside the fan is a bounded flow. Due to the presence of the motor-impeller-stator system in the base, the internal flow has the flow characteristics similar to that of a rotating machinery (Gammack et al., 2012). The flow outside the fan consists of the jet blown out from the wind channel's slit and the entrained flow around the fan. The jet is constrained by the surface near the slit, forming the Coanda effect.

Figure 1.2 illustrates the flow characteristic of the bladeless fan. In addition, the total mass flow rate at downstream can be calculated by:

$$Q_{total} = Q_{jet} + Q_{entrained}$$

where

$$Q_{jet} = Q_{inlet}$$

$$Q_{entrained} = Q_{back} + Q_{side}$$

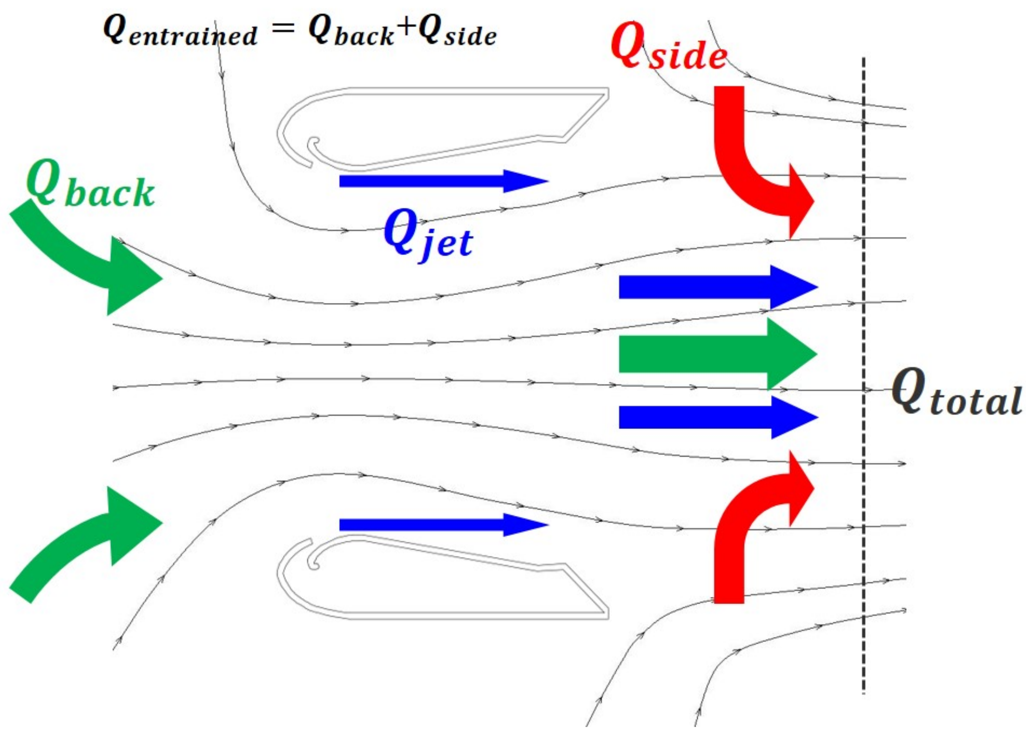

Figure 1.3. Schematic of the flow outside the bladeless fan

1.1.2 Research of the Bladeless Fan

Bladeless fans generate jet flow with the help of Coanda effect through the wind channel. Jet flow has been widely used in nozzles, jet engine, active control technique on the airfoil and other devices involving fluid injection and many research have been carried out. Zhang et al. (Zhang et al., 2012) studied synthetic jet circulation control technology to enhance the lift of an airfoil. A two-dimensional unsteady Reynolds-averaged Navier-stokes simulation is used to investigate the effect of synthetic jet circulation control on NCCR1510-7067N airfoil. The results illustrate that synthetic jet is able to effectively delay the flow separation on the airfoil trailing edge and to increase the circulation over the airfoil by Coanda effect.

Howe investigated the noise generated by a Coanda wall jet circulation control device by analytical research (Howe, 2002) in which a 2D circulation control (CC-) hydrofoil was employed. It is found that the noise produced by a circulation control device consists of curvature noise, jet slot noise and passive slot noise. Curvature noise generated by the interaction of boundary layer turbulence with the rounded trailing edge of the CC-hydrofoil is the main source at very low frequencies. The jet slot noise dominates at higher frequencies; Passive slot noise caused by the scattering by the slot lip of nearfield pressure fluctuations in the turbulent boundary layer of the exterior mean flow past the slot is comparable to the conventional sharp edged trailing edge noise.

Wetzel et. al.,(Wetzel et al., 2009) studied the acoustic characteristics of a circulation control airfoil by experiments and it validated Howe's results. It is illustrated that the main noise source is located at the slit. In addition, the flow separation causes a loud noise, but this kind of noise is able to be eliminated by increasing jet velocity. However, with the increase of the jet velocity, the overall noise level increases.

The Coanda surface adjacent the slit of the bladeless fan is a crucial structure to keep the air jet attached to the convex surface, delaying the flow separation (Gammack et al., 2012). Thus, the outflow produced by the bladeless fan is much more uniform than that of the conventional fan. Li et al. (Li et al., 2014) investigated the influence of Coanda surface's curvature on the aerodynamic performance of bladeless fans by conducting two-dimensional and three-dimensional numerical simulations. Coanda surface with five different curvatures was investigated. It was found that the magnitude of curvature affects the flow direction and an optimal curvature keeps the outflow attached to the surface. Simulation results show that a low-pressure region exists near the outlet. With the increase of the Coanda surface's curvature, several separated low-pressure regions gradually enlarges, merging slowly and finally form a large low pressure region.

To investigate the flow structure outside a circular bladeless fan and the influence of Reynolds number, Li et al. (Li et al., 2016) conducted experiments by using constant temperature anemometer (CTA) hot-wire system. It is shown that the time-averaged velocity and turbulence intensity increase with increased Reynolds number. The complete flow field structure is shown in Fig. 1.4, where the annular jet is injected outward from the annular slit, entraining the ambient air. The entire outflow field shows symmetry in a horizontal direction. At near field, the flow structure consists of two separated peak. As far away from the bladeless fan, the annular jet starts to converge and at far field and the flow develops into a classical single jet.

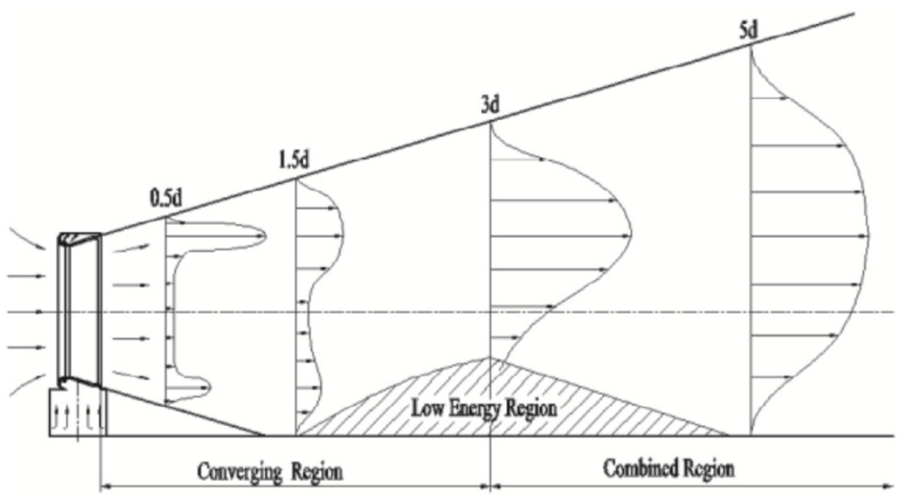

Figure 1.4. Sketch of the outflow field structure for the bladeless fan (Li et al., 2016)

Jafari et al.(Jafari et al., 2015) employed a numerical method to evaluate aerodynamic and acoustic performance of the bladeless fan with a circular wind channel.

It is reported that the outlet air velocity at the top is larger than that at the bottom. In addition, with an increase of inlet volume flow rate, the outlet volume flow rate increase linearly, but the generated noise level also increases at the same time. Therefore, to design the bladeless fan, a compromise between the increased inlet flow rate and reduced noise level is required. The main noise source is also predicted. As shown in Fig. 1.5, the output slit is the predominant noise source. It is caused by high pressure gradient and vorticity gradient at the slit (Jafari et al., 2015).

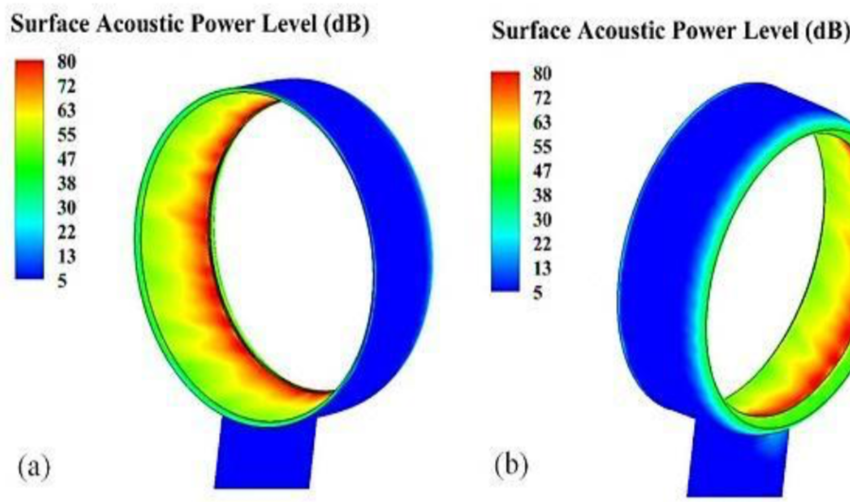

Figure 1.5. Sound Power contour at (a) front side (b) back side of the bladeless fan (Jafari et al., 2015).

Jafari et al.(Jafari et al., 2016) studied the effect of geometric parameters on the aerodynamic performance of bladeless fans. The discharge ratio, defined by the ratio of outflow rate to inlet flow rate, Q_{out}/Q_{inlet}, is applied to evaluate aerodynamic performance of the bladeless fan. The slit width is identified as the most influential parameters. The discharge ratio increases significantly by narrowing the slit. A circular fan with a cross-section height of 3cm and outlet angle of 16 ° yields the optimal aerodynamic performance. Furthermore, the aspect ratio, defined as the ratio of the wind channel's height to its width, affects aerodynamic performance of bladeless fans. When the aspect ratio is higher than 1, the discharge ratio decreases. The shape of the wind channel is also investigated. At high aspect ratios, the discharge ratio of the circular fan is greater than that of the rectangular fan.

Jafari et al. (Jafari et al., 2017) carried out numerical simulations to investigate the influence of geometric parameters on acoustic performance. Sound pressure level (SPL) and overall sound pressure level (OASPL) diagrams are illustrated to evaluate the noise generated by the bladeless fan with different geometric parameters. It is found that with the decrease of the cross-sectional height of the wind channel, the generated noise decrease. The results obtained by different outlet angle show that the noise produced by the bladeless fan increases by increasing the outlet angle. Similar to the effect on aerodynamic performance, the slit width has the greatest impact on the acoustic performance. The generated noise increases significantly with decreased slit width. As for the aspect ratio and shape of the wind channel, the rectangular wind channel with the aspect ratio of 1 (i.e., a square) has the best acoustic performance.

1.2 Principle of CFD Simulation

In the context of studying bladeless fans, the flow can be treated as incompressible flow without heat transfer. Then velocity $\mathbf{u}(\mathbf{x}, t)$ and pressure $\mathbf{p}(\mathbf{x}, t)$ are described by the incompressible Navier-Stokes equations,

$$\frac{\partial u_i}{\partial x_i} = 0, \tag{1.1}$$

$$\frac{\partial u_i}{\partial t} + u_j \frac{\partial u_i}{\partial x_j} = -\frac{1}{\rho}\frac{\partial p}{\partial x_i} + \frac{\partial}{\partial x_j}\left[\nu\left(\frac{\partial u_i}{\partial x_j} + \frac{\partial u_j}{\partial x_i}\right)\right], \tag{1.2}$$

where ρ is fluid density and ν is kinematic viscosity.

In computational fluid dynamics (CFD), Reynolds-Averaged Navier-Stokes (RANS) simulation is frequently used for the steady state, and Large Eddy Simulation (LES) is conducted for the transient unsteady state (Wilcox, 1998) (Ferziger and Peric, 2012).

1.2.1 Reynolds-Averaged Navier-Stokes Simulation

In RANS, every flow variable ϕ is decomposed into a time-averaged part and a time varying fluctuation:

$$\phi(x_i, t) = \overline{\phi}(x_i) + \phi'(x_i, t), \tag{1.3}$$

where

$$\overline{\phi}(x_i) = \lim_{T\to\infty} \frac{1}{T}\int_0^T \phi(x_i, t)dt. \tag{1.4}$$

Here, t is time and T is the averaging interval. This interval must be large compared to the time scale of fluctuations and then $\overline{\phi}$ is independent of time. From Eq. 1.3, it follows that $\overline{\phi'} = 0$. Thus, averaging any linear term in the conservation equations simply gives the identical term for the averaged quantity. A quadratic nonlinear term can be expressed by:

$$\overline{u_i\phi} = \overline{(\overline{u}_i + u_i')(\overline{\phi} + \phi')} = \overline{u}_i\overline{\phi} + \overline{u_i'\phi'}. \tag{1.5}$$

The velocity and pressure are then expressed by:

$$u(x_i, t) = \overline{u}(x_i) + u'(x_i, t), \tag{1.6}$$

$$p(x_i, t) = \overline{p}(x_i) + p'(x_i, t). \tag{1.7}$$

Furthermore, the time-averaged velocity $\overline{u}_i$ and $\overline{p}$ can be solved by the Reynolds-Averaged Navier-Stokes equation,

$$\frac{\partial \overline{u}_i}{\partial x_i} = 0, \tag{1.8}$$

$$\frac{\partial \overline{u}_i}{\partial t} + \overline{u}_j\frac{\partial \overline{u}_i}{\partial x_j} = -\frac{1}{\rho}\frac{\partial \overline{p}}{\partial x_i} + \frac{\partial}{\partial x_j}\left[\nu\left(\frac{\partial \overline{u}_i}{\partial \overline{x}_j} + \frac{\partial \overline{u}_j}{\partial x_i}\right)\right] - \frac{\partial\left(\overline{u_i'u_j'}\right)}{\partial x_j}, \tag{1.9}$$

where $\tau_{ij} = -\rho\overline{u_i'u_j'}$ is the Reynolds stress. Thus, τ_{ij} is a symmetric tensor and therefore has six independent components. In RANS equations Eq. 1.8 and Eq. 1.9, there are four unknowns of interest, i.e. the averaged pressure $\overline{p}$ and three averaged velocity components $\overline{\mathbf{u}}$. The six Reynolds stress components present six extra unknowns in RANS equations. However, since there are only four equations, including a continuity equation Eq. 1.8 and three momentum conservation equations Eq. 1.9, the RANS equations are not closed. In order to close the system, additional equations are required.

A common approach is to model the Reynolds stresses. For example, Boussinesq hypothesis relates the Reynolds stresses to the mean velocity gradients,

$$-\rho\overline{u_i'u_j'} = \mu_t(\frac{\partial u_i}{\partial x_j} + \frac{\partial u_j}{\partial x_i}) - \frac{2}{3}(\rho k + \mu_t \frac{\partial u_k}{\partial x_k})\delta_{ij}, \tag{1.10}$$

where μ_t is turbulent eddy viscosity. The Boussinesq hypothesis is employed in the popularly used in Spalart-Allmaras model, the $k-\epsilon$ models and the $k-\omega$ models, etc. (Ferziger and Peric, 2012). The advantage of this approach is the relatively low computational cost associated with the computation of the turbulent viscosity, μ_t. The disadvantage is that μ_t is assumed as an isotropic scalar quantity, which is not strictly true (Fluent, 2011).

In the present study, the standard $k-\epsilon$ model is applied in RANS simulations. k is the turbulence kinetic energy and ϵ presents the turbulence dissipation rate, which is defined by,

$$k = \frac{1}{2}\overline{u_i'u_i'} \tag{1.11}$$

and

$$\epsilon = \nu\overline{\frac{\partial u_i'}{\partial x_k}\frac{\partial u_i'}{\partial x_k}} \tag{1.12}$$

In $k-\epsilon$ model, k and ϵ are solved by their transport equations:

$$\frac{\partial}{\partial t}(\rho k) + \frac{\partial}{\partial x_i}(\rho k u_i) = \frac{\partial}{\partial x_j}\left[\left(\mu + \frac{\mu_t}{\sigma_k}\right)\frac{\partial k}{\partial x_j}\right] + G_k + G_b - \rho\epsilon - Y_M \tag{1.13}$$

and

$$\frac{\partial}{\partial t}(\rho\epsilon) + \frac{\partial}{\partial x_i}(\rho\epsilon u_i) = \frac{\partial}{\partial x_j}\left[\left(\mu + \frac{\mu_t}{\sigma_\epsilon}\right)\frac{\partial \epsilon}{\partial x_j}\right] + C_1\frac{\epsilon}{k}(G_k + C_{3\epsilon}G_b) - C_{2\epsilon}\rho\frac{\epsilon^2}{k}. \tag{1.14}$$

Here, G_k is the production of turbulence kinetic energy due to the mean velocity gradients, which can be calculated by an exact equation:

$$G_k = -\rho\overline{u_i'u_j'}\frac{\partial u_j}{\partial x_i} \tag{1.15}$$

It can also be evaluated in a manner consistent with the Boussinesq hypothesis,

$$G_k = \mu_t S^2 \tag{1.16}$$

where S is the modulus of the mean rate-of-strain tensor,

$$S = \sqrt{2S_{ij}S_{ji}} \tag{1.17}$$

G_b in Eq. 1.13 and Eq. 1.14 is the production of turbulence kinetic energy due to buoyancy and it is usually included when the flow field have both a non-zero gravity and a non-zero temperature gradient,

$$G_b = \beta g_i \frac{\mu_t}{Pr_t} \frac{\partial T}{\partial x_i} \tag{1.18}$$

where Pr_t is the turbulent Prandtl number for energy and its default value is 0.85. g_i is the component of the gravitational acceleration in the ith direction. β is the coefficient of thermal expansion,

$$\beta = -\frac{1}{\rho}\left(\frac{\partial \rho}{\partial T}\right)_p \tag{1.19}$$

$C_{3\epsilon}$ in Eq. 1.14 determines the degree to which ϵ is affected by the buoyancy and is given by the following equation:

$$C_{3\epsilon} = \tanh\left|\frac{v}{u}\right| \tag{1.20}$$

where v is the component of the flow velocity parallel to the gravitational vector and u is the component of the flow velocity perpendicular to the gravitational vector.

Y_M in Eq. 1.13 represents the contribution of the fluctuating dilatation in compressible turbulence to the overall dissipation rate, which is only considered in high-Mach-number compressible flow. This term is modeled by:

$$Y_M = 2\rho\epsilon M_t^2 \tag{1.21}$$

where M_t is the turbulent Mach number and given by:

$$M_t = \sqrt{\frac{k}{a^2}} \tag{1.22}$$

where a is the speed of sound.

The constants in Eq. 1.13 and Eq. 1.14 have the following default values (Moukalled et al., 2016):

$$C_{1\epsilon} = 1.44; C_{2\epsilon} = 1.92; \sigma_k = 1.0; \sigma_\epsilon = 1.3$$

The turbulent viscosity μ_t is modeled by:

$$\mu_t = \rho C_\mu \frac{k^2}{\epsilon} \tag{1.23}$$

where C_μ=0.09. All constants mentioned above are determined from experiments with air and water for fundamental turbulent shear flows including homogeneous shear flows and decaying isotropic grid turbulence (Moukalled et al., 2016).

1.2.2 Large Eddy Simulation

In RANS simulations, only time-averaged flow variables are taken into consideration. However, eddies may affect the flow characteristic significantly. The large scale motions are generally much more energetic than the small scale ones. Their size and strength make them by far the most effective transporters of the conserved properties. Thus, a simulation which treats the large eddies more exactly than the small ones may be more effective. Large eddy simulation (LES) is just such an approach (Ferziger and Peric, 2012). Compared to RANS, LES is much more computationally expensive, but it is more accurate in most cases (Sagaut, 2006).

In LES, a spatial filter is applied to relate the large scale components of the total field, which is essentially a local average of the complete field. The spatial filter is used to decompose the flow parameter $\phi(\mathbf{x}, t)$ into a filtered part

$$\tilde{\phi}(\mathbf{x}, t) = \int G(\mathbf{x}', \mathbf{x})\phi(\mathbf{x} - \mathbf{x}', t)d\mathbf{x}' \tag{1.24}$$

and a subgrid scale (SGS) part

$$\tilde{\phi}^{sgs}(\mathbf{x}, t) = \phi(\mathbf{x}, t) - \tilde{\phi}(\mathbf{x}, t) \tag{1.25}$$

where $G(\mathbf{x}', \mathbf{x})$ is the filter kernel. Popularly used filter kernels include Gaussian, box filter (a simple local average) and cutoff filter (a filter which eliminates all Fourier coefficients belonging to wavenumbers above a cutoff one) (Ferziger and Peric, 2012). Every filter has length scale, Δ. Roughly, eddies of size larger than Δ are large eddies while those smaller than Δ are small eddies, the ones to be modeled (Wilcox, 1998).

The filtered Navier-Stokes equations for incompressible flow can be obtained by filtering the standard incompressible Navier-Stokes equation,

$$\frac{\partial \tilde{u}_i}{\partial x_i} = 0, \tag{1.26}$$

$$\frac{\partial \tilde{u}_i}{\partial t} + \tilde{u}_j \frac{\partial \tilde{u}_i}{\partial x_j} = -\frac{1}{\rho}\frac{\partial \tilde{p}}{\partial x_i} + \frac{\partial}{\partial x_j}\left[\nu\left(\frac{\partial \tilde{u}_i}{\partial x_j} + \frac{\partial \tilde{u}_j}{\partial x_i}\right)\right] - \frac{1}{\rho}\frac{\partial \tau_{ij}}{\partial x_j}. \tag{1.27}$$

Here,subgrid-scale stress is $\tau_{ij} = -\rho(\widetilde{u_i u_j} - \tilde{u}_i\tilde{u}_j)$, which presents additional unknowns.

The subgrid-scale stress contains local averages of the small scale field so models for it should be based on the local velocity field or, probably, on the past history of the local fluid. The latter can be accomplished by using a model that solves partial differential equations to obtain the parameters needed to determine the SGS stress (Moukalled et al., 2016).

Due to the presence of the subgrid-scale stress, the filtered Navier-Stokes equations are not closed, so additional equations are required. The most widely used subgrid model is one introduced by Smagorinsky (Lilly, 1966) (Smagorinsky, 1963), which is an eddy viscosity model,

$$\tau_{ij} - \frac{1}{3}\tau_{kk}\delta_{ij} = \mu_t\left(\frac{\partial \tilde{u}_i}{\partial x_j} + \frac{\partial \tilde{u}_j}{\partial x_i}\right) = 2\mu_t \tilde{S}_{ij} \tag{1.28}$$

where μ_t is the eddy viscosity and $\tilde{S}_{ij}$ is the fitlered strain rate. The form of the subgrid-scale eddy viscosity can be derived by dimensional arguments:

$$\mu_t = C_s^2 \rho \Delta^2 |\tilde{S}| \tag{1.29}$$

where C_S is a model parameter to be determined, Δ is the filter length scale and $|\tilde{S}| = \sqrt{\tilde{S}_{ij}\tilde{S}_{ji}}$ (Canuto and Cheng, 1997).

1.2.3 CFD Flow Solver

There are two types of solver applied in computational fluid dynamic, the pressure-based approach and the density-based approach. The pressure-based approach is mainly applied for low-speed incompressible flows, while the density-based approach is usually used for high-speed compressible flows. However, both methods have been extended and reformulated to solve for a wide range of flow conditions. (Ferziger and Peric, 2012).

In both approaches, the velocity field is computed from the momentum equations. In the pressure-based approach, the pressure field is obtained by solving a pressure or pressure correction equation which is obtained by manipulating continuity and momentum equations. In the density-based approach, the density field is extracted by solving the continuity equation and the pressure field which is obtained by the equation of state (Moukalled et al., 2016).

Since the flow inside and around the bladeless fan is low-speed and incompressible, the pressure-based approach is employed in the present study. The pressure-based solver applies an algorithm which belongs to the projection method. In the projection method, the constraint of continuity of the velocity field is extracted by solving a pressure or pressure correction equation (Ferziger and Peric, 2012). The pressure equation is derived from the continuity and the momentum equations in such a way that the velocity field, corrected by the pressure, satisfies the continuity. Since the governing equations are nonlinear and coupled each other, the solution process involves iterations in which the entire set of governing equations is solved repeatedly until the solution converges. The segregated algorithm and the coupled algorithm are two types of algorithm for pressure-based solver. In the segregated algorithm, the governing equations are solved one after another. Since the governing equations are non-linear and coupled, the solution loop has to be carried out iteratively to obtain a converged numerical solution (Ferziger and Peric, 2012).

In the segregated algorithm, the individual governing equations for the variables, e.g., velocity, pressure, temperature, are solved sequentially. Each governing equation is decoupled from other equations. The advantage of the this algorithm is memory-efficient because the discretized equations only need to be stored in the memory one at a time. However, the solution convergence speed is relatively low because the equations are solved in a decoupled manner. The procedures of the segregated algorithm are outlined below (Fluent, 2011):

(i) Update fluid properties accoriding to the current solution.

(ii) Solve the momentum equations sequentially, using the recently obtained values of flow properties, i.e.,pressure and mass fluxes.

(iii) Solve the pressure correction equation by using the recently updated velocity field and the mass-flux.

(iv) Correct pressure, velocity field and face mass fluxes by using the pressure correction obtained from Step (iii).

(v) Solve the equations for additional scalars, including turbulent quantities and energy, by using the current values of the solution variables.

(vi) Update the source terms arising from the interactions among different phases.

(vii) Check for the convergence of the equations.

(viii) Repeat the above steps until the solution is convergent.

The coupled algorithm is another algorithm for the pressure-based solver. The semi-implicit pressure-coupled equations are widely used in CFD software. This algorithm solves a coupled system of equations comprising the momentum equations and the continuity equation. The procedure of the coupled algorithm is,

(i) Update fluid properties based on the current solution.

(ii) Solve the momentum equations and continuity equation simultaneously.

(iii) Update mass flux.

(iv) Solve the equations for additional scalars, including turbulent quantities and energy, using the current values of the solution variables.

(v) Check for the convergence of the equations.

Since the momentum and continuity equations are solved in a coupled manner, compared to the segregated algorithm, the convergence speed of the solution is improved. However, the shortcoming of this approach is that the memory requirement increases significantly because the discrete system of momentum and continuity equations need to be stored in the memory when solving for the pressure and velocity fields.

In the present study, Semi-Implicit Method for Pressure-Linked Equations (SIMPLE) algorithm is used. SIMPLE algorithm is a type of pressure-based coupled algorithm and was proposed by Patankar and Spalding in 1972 (Patankar and Spalding, 1983). Since the inception of SIMPLE algorithm, it is widely used in CFD and computational heat transfer and it becomes a main method to solve the problems of incompressible flows. Subsequently, this algorithm was improved and successfully applied to the computation of compressible flows.

The fundamental assumption of SIMPLE algorithm is that velocity field and pressure field are independent of each other. Another assumption is that the influence of velocity corrections at different locations is neglected. The procedure of SIMPLE algorithm is outlined below (Fluent, 2011):

(i) Assume a velocity distribution to calculate the coefficients and constants of the momentum equation for the first iteration.

(ii) Assume a pressure field.

(iii) calculate the coefficients and constants of the discrete equations.

(iv) Solve the momentum equation.

(v) Solve pressure-correction equation based on the velocity field.

(vi) Correct pressure and velocity.

(vii) Solve others discrete transport equations.

(viii) Check for the convergence of the equations.

The main idea of SIMPLE algorithm is assumption and correction. Since the assumption may be not accurate, the obtained velocity field may not satisfy the continuity equation. Thus, the correction of the pressure field is required. The principle of the correction is that the velocity field obtained by corrected pressure field is able to satisfy the discrete continuity equation. According to this principle, the pressure and velocity predicted by the discrete momentum equation are substituted into the discrete continuity equation, then the pressure-correction equation can be obtained and the correction value of pressure can be computed. The updated velocity field is able to be calculated by the corrected pressure field. The steps above are iterated until the velocity field is convergent.

1.3 Principle of Acoustic Simulation

In the present study, aerodynamic noise generated by the bladeless fan is investigated. Aerodynamic noise refers to the noise caused by air flow or air disturbance caused by a moving object in the air. There are three types of noise sources of aerodynamic noise, including monopole, dipole and quadrupole (Kinsler et al., 1999).

Monopole source, also known as pulsating noise source, is caused by uneven mass or heat inflow into the air. The monopole is like a pulsating sphere, and the wavefronts which cause sound wave are in the same phase, so the directivity of the monopole is a sphere. However, the radiation of the monopole has no directivity (Kinsler et al., 1999).

The dipole source is formed by the unstable reaction between the fluid and the object when there are obstacles in the fluid. The simplest dipole source consists of two monopoles with equal strength placed an infinitesimally short distance apart, operating at the same frequency but always vibrating 180° out of phase with each other (Kinsler et al., 1999). The vortex shedding at the blade or airfoil trailing edge is a typical dipole source (Crighton, 1975).

The quadrupole is formed by sound waves radiated by viscous stress, without mass or heat injection or obstacles in the air. It is one kind of stress sources (Kinsler et al., 1999). Subsonic turbulent noise is the most common quadrupole source (Crighton et al., 1992).

The noise sources of the bladeless fan include noise generated from the motor, rotating rotor, airflow and vibration of the structure. The noise produced by the motor is electromagnetic noise and will not be investigated in the present study. The noise produced by the rotor includes discrete noise and broadband turbulence noise. The noise generated by airflow is broadband turbulence noise (Schmalz and Kowalczyk, 2015). Passive noise cancellation method is applied by Dyson fan to reduce the noise generated from the rotating rotor and 75% noise has been reduced (Gammack et al., 2012). In the present study, numerical method is employed to investigate the aerodynamic noise generated from each part of the bladeless fan and the effect of geometric parameters on airflow noise.

The methods to solve aerodynamic noise include the direct method, aeroacoustic analogy, and broadband noise source models. In direct method, acoustic equations are solved directly. This approach has high requirement on mesh, so it is very computationally expensive. Aeroacoustic analogy is based on the transient solution of flow field to extract sound source and then calculate sound propagation. Broadband noise source models are based on the steady solution of the flow field to determine the position of the noise source (Mohamud and Johnson, 2006).

In 1952, Lighthill rearranged the Navier- Stokes equations, which govern the flow of a compressible viscous fluid, into an inhomogeneous wave equation, thereby making a connection between fluid mechanics and acoustics. This is called Lighthill analogy (Powell, 1964) (Lighthill, 1952).

The Navier-Stokes equations for compressible flow are:

$$\frac{\partial \rho}{\partial t} + \frac{\partial}{\partial x_i}(\rho u_i) = 0 \tag{1.30}$$

and

$$\frac{\partial}{\partial t}(\rho u_i) + \frac{\partial}{\partial}(\rho u_i u_j) = \frac{\partial}{\partial x_i}(-p\delta_{ij} + \tau_{ij}) \tag{1.31}$$

where δ_{ij} is the Kronecker delta, and τ_{ij} is the viscous stress tensor.

Based on Navier-Stokes equations above, Lighthill's equation can be derived:

$$\left(\frac{\partial^2}{\partial t^2} - c_0^2 \frac{\partial^2 \rho}{\partial x_i^2}\right)(\rho - \rho_0) = \frac{\partial^2}{\partial x_i \partial x_j}\left[\rho u_i u_j + (p - c_0^2 \rho)\delta_{ij} - \tau_{ij}\right] \tag{1.32}$$

Here, the Lighthill stress tensor is introduced and given by,

$$T_{ij} = \rho u_i u_j + (p - c_0^2 \rho)\delta_{ij} - \tau_{ij} \tag{1.33}$$

Each of the acoustic source terms in T_{ij} plays a significant role in noise generation; $\rho u_i u_j$ describes unsteady convection of flow; τ_{ij} describes sound generated by viscous forces, and $(p - c_0^2 \rho)\delta_{ij}$ describes non-linear acoustic generation processes.

The limit of Lighthill analogy is that it can only be used to solve the fluid in a free space. In 1955, Curle develops Lighthill's theory so that the analogy is able to be applied to cases with solid and stationary boundary (Curle, 1955). In Curle's analogy, the solid boundary is described by $f(\mathbf{x}) = 0$, and then Heaviside function is introduced,

$$H(f) = \begin{cases} 1 & \text{for } x_i \text{ outside } f \\ 0 & \text{for } x_i \text{ inside } f \end{cases} \tag{1.34}$$

Apply Heaviside function in Navier-Stokes equations for compressible flow, the Curle's equation can be obtained:

$$\left(\frac{\partial^2}{\partial t^2} - c_0^2 \frac{\partial^2 \rho}{\partial x_i^2}\right)[(\rho - \rho_0)H] = \frac{\partial}{\partial t}\left(\rho u_i \frac{\partial H}{\partial x_i}\right) - \frac{\partial}{\partial x_i}\left(T_{ij}\frac{\partial H}{\partial x_j}\right) + \frac{\partial^2}{\partial x_i \partial x_j}(T_{ij}H) \tag{1.35}$$

In 1969, Ffowcs Willams and Hawkings extended Curle's analogy to a more general Ffowcs Willams and Hawkings (FW-H) equation, which can be used to solve the case with moving solid boundary (Ffowcs Williams and Hawkings, 1969). When the solid boundary is moving with U_i, $\frac{\partial H}{\partial t} = 0$. Eq. 1.35 becomes:

$$\left(\frac{\partial^2}{\partial t^2} - c_0^2 \frac{\partial^2 \rho}{\partial x_i^2}\right)[(\rho - \rho_0)H] = \frac{\partial}{\partial t}\left((\rho(u_i - U_i) + \rho_0 U_i)\frac{\partial H}{\partial x_i}\right) - \frac{\partial}{\partial x_i}\left(T_{ij}\frac{\partial H}{\partial x_j}\right) + \frac{\partial^2}{\partial x_i \partial x_j}(T_{ij}H) \tag{1.36}$$

Farasset and Brentner (Farassat, 2007)(Brentner and Farassat, 2003) developed the solution of FW-H analogy, in which only the surface integrals are taken into consideration and quadrupole sources are neglected. Sound pressure can be divided into thickness noise, $p'_T(x,t)$ and loading noise, $p'_L(x,t)$, i.e.,

$$p'(x,t) = p'_T(x,t) + p'_L(x,t), \tag{1.37}$$

and

$$p'_T(x,t) = \frac{1}{4\pi}\int_{f=0}\left[\frac{\rho_0(\dot{v}_n + v_{\dot{n}})}{r(1-M_r)^2}\right]_\tau dS + \frac{1}{4\pi}\int_{f=0}\left[\frac{\rho v_n(r\dot{M}_r + cM_r - cM^2)}{r^2(1-M_r)^3}\right]_\tau, \tag{1.38}$$

and

$$p'_L(x,t) = \frac{1}{4\pi c}\int_{f=0}\left[\frac{\dot{l}_r}{r(1-M_r)^2}\right]_\tau dS + \frac{1}{4\pi}\int_{f=0}\left[\frac{l_r - l_M}{r(1-M_r)^2}\right]_\tau + \frac{1}{4\pi c}\int_{f=0}\left[\frac{l_r(r\dot{M}_r + cM_r - cM^2}{r(1-M_r)^3}\right]_\tau, \tag{1.39}$$

where

$$\tau = t - \frac{r}{c_0},$$
$$v_n = \left[v_i + \frac{\rho}{\rho_0}(u_i - v_i)\right] n_i,$$
$$l_i = P_{ij}n_j.$$

In the equations above the variables with a dot are the source time derivatives of those variable. M denotes the surface velocity vector normalized by the speed of sound. The subscripts n and r implies the dot product with the unit normal vector or the unit radiation vector, respectively.

1.4 Motivation for Research

Most of the previous researches focus on circular fans with an aspect ratio of 1. However, increasing the aspect ratio may improve the aerodynamic performance(Jafari et al., 2016). In this study, a bladeless fan model with high aspect ratio is investigated. The performance of the bladeless fan is very sensitive to the design details. Although the effect of slit width and cross-section height on performance has been investigated previously, their effects on flow structure and influence zones are not illustrated. In addition, there were few studies on the influence of geometric parameters on acoustic performance and noise source. Thus, the detailed aerodynamic and aeroacoustic characteristic is presented in this study, which will help the improved design of the next-generation bladeless fan.

1.5 Research Objective

In the present study, a combined numerical and experimental study is reported. Steady and transient CFD simulations are used to predict aerodynamic performance of the bladeless fan. Then, based on transient CFD results, computational aeroacoustic method is employed to calculate the noise generated by the bladeless fan and identify the main noise source. The simulations of the wind channel with different design are carried out to investigate the influence of geometric parameters on bladeless fan's performance.

1.6 Outline of the Thesis

The methodology, including details of numerical simulation and experiments setup, is presented in chapter 2. Validation of numerical results is given in section 3. Chapter 4 illustrates the flow characteristic of the bladeless fan by velocity contours and velocity profiles. In addition, the effect of geometric parameters on aerodynamic performance is presented. In chapter 5, aeroacoustic analysis is reported. Sound pressure level is investigated to evaluate acoustic performance of the bladeless fan. Similarly, the influence of geometric parameters is investigated. Finally, conclusions and suggestions of future work are given in chapter 6.

2. METHODOLOGY

In the present study, both numerical and experimental studies are carried out for a prototype of a bladeless fan baseline model and its variation.

2.1 Experimental Set-up

In the present study, experiments are conducted to validate the numerical results. Air velocity measurement is conducted to verify aerodynamic results. The bladeless fan is placed in the center of a room of 13m×8.5m×6.7m so that the influence of the surrounding hard wall on the wind generated by the fan can be neglected. A three-dimensional ultrasonic anemometer (Model DA-600) is used to measure air velocity at $x = 1.5$m, illustrated in Fig.2.1(a). A two-dimensional robotic scanner is used to translate the anemometer to different measurement positions automatically. Figure 2.1(b) shows the 3D anemometer fixed on the scanner. More than 800 measurement positions are selected. The range along vertical direction Z is from 0.1m to 1.4m with a resolution of 0.1m; while the range along horizontal direction is from -0.5m to 0.5m and the resolution is 0.01m. At each position, measurements last 30 seconds and the sampling rate 1s. The time-averaged velocity components are calculated.

Sound pressure is measured to validate aeroacoustic simulations. The experiments are conducted in an anechoic chamber in Ray W. Herrick Laboratories of Purdue University. A B&K intensity probe is mounted on the two-dimensional robotic scanner, as shown in Fig. 2.2(a). The intensity probe (B&K 2270-S), as illustrated in Fig. 2.2(b), is covered by a wind shield to eliminate the effect of the powerful wind. The sound pressure measurements are conducted at 9 measurement positions. All positions are located in the center plane ($y = 0$) of the bladeless fan at three different

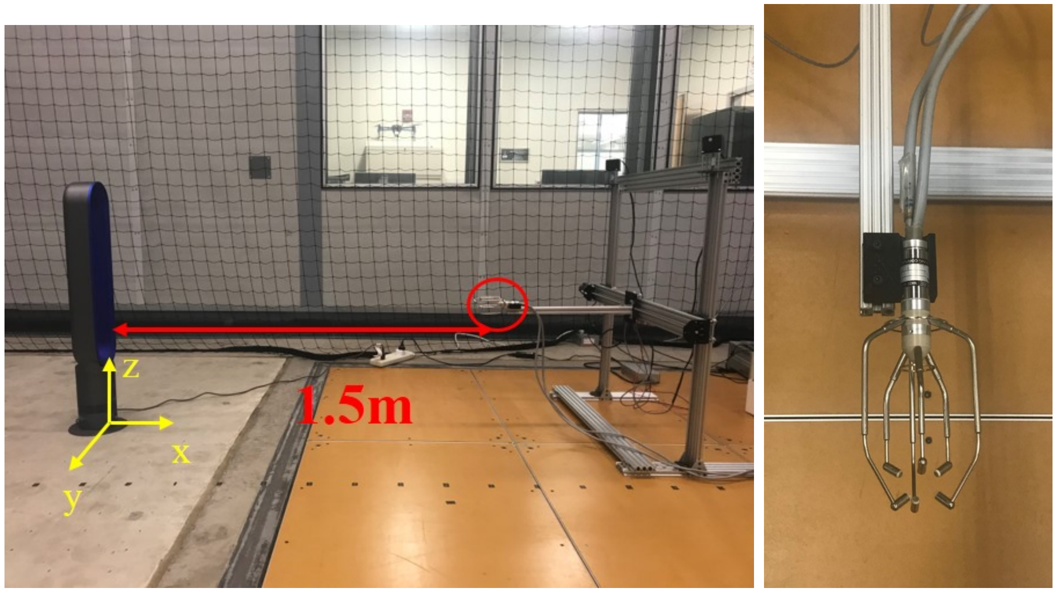

(a) (b)

Figure 2.1. (a) Air velocity measurement set-up. (b) 3D ultrasonic anemometer

heights, z =0.3m, 0.55m and 0.8m, respectively, and their distances away from the fan is x = 0.1m, 0.5m and 1.5m, respectively.

Contours and profiles of the measured velocity are used to validate aerodynamic results while sound pressure level is employed to verify the aeroacoustic results, which will be presented in Chapter 3.

To determine the boundary conditions of simulations, air velocity measurement at wind channel inlet and pressure measurement at the intake are conducted. The pressure at the fan intake is measured by a digital manometer, as shown in Figure.2.3. The measured pressure is used to define the boundary condition for the simulations for the entire fan prototype.

When investigating the influence of the geometric parameters of the wind channel, the base with rotor and stator are neglected. The mass flow rate at the intake is used to define the boundary condition. To calculate the inlet mass flow rate, the velocity magnitude at the wind channel inlet is measured. Figure. 2.4(a) illustrates the experimental set-up of velocity measurement at wind channel inlet. Two dimensional

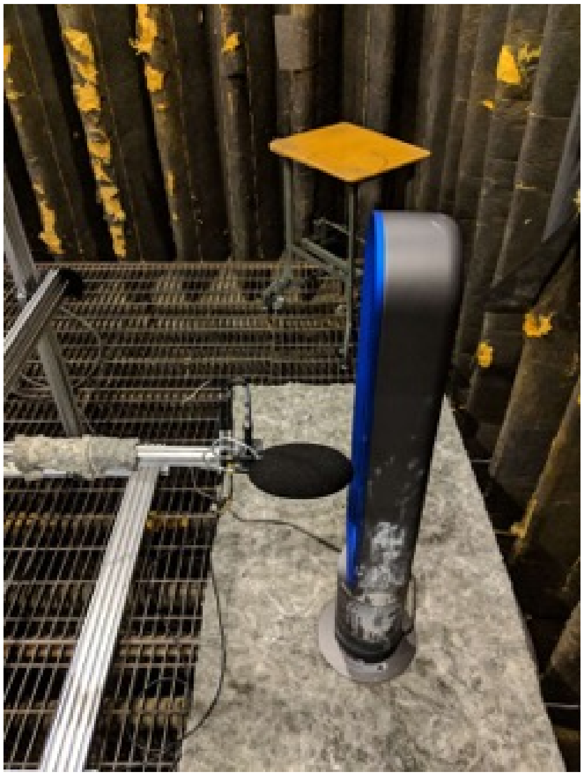

(a)

(b)

Figure 2.2. (a) Sound pressure measurement set-up. (b) Intensity probe

hotwire anemometer is applied to measure velocity magnitude and the velocity profile is obtained, which is used as the boundary condition for simulations.

2.2 Geometric Model of the Bladeless Fan

The details of the baseline wind channel is illustrated in Fig. 2.5(a)with a height and width of 0.76m and 0.17m, respectively. The corresponding aspect ratio is 4.5. There are five small blocks set near the slit on each side, and the spacing between each block is 10cm. At the top of the wind channel, a block with 12 perforations is set on each side so that the air is able to penetrate the block and enter the top part.

The structure of the base is simplified, as shown in Fig. 2.5(b). For the prototype, there are 12 separated square inlets with perforated patterns. In the simulation,

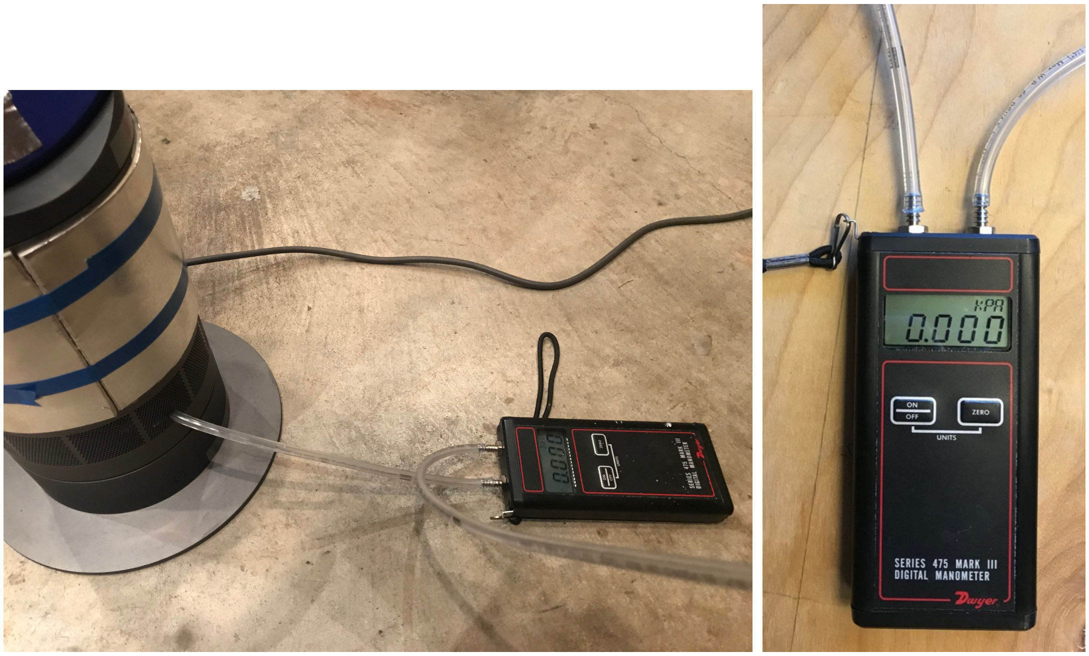

(a) (b)

Figure 2.3. (a) Pressure measurement at the intake. (b) Digital manometer.

details of the perforated structure are neglected so the inlet is of a cylindrical shape. Inside the base, only the air handling parts, i.e, the rotor and the stator are taken into consideration

2.3 Numerical Set-up

The fan prototype is set in a computational domain (4m $\times$ 2m $\times$ 2m), as shown in Fig.2.6(a). When characterizing the aerodynamic and aeroacoustic performances of the bladeless fan, the fan model with rotor and stator in the base is employed. When investigating the influence of geometric parameters of the wind channel on aerodynamic and aeroacoustic performance, on the other hand, the motor and impellers are not included in the simulation. Figure 2.6(b) illustrates the cross-section of the baseline model with details listed in Table 2.1.

(a) (b)

Figure 2.4. (a) Velocity measurement at wind channel inlet. (b) Hotwire anemometer.

Table 2.1. Parameters of the cross-section of the baseline wind channel

Geometric parameter	Value
Chord of cross-section, c	12cm
Width of slit, d	2mm
Height of cross-section, H	3cm
Location of slit, x_0	1.2cm

The hybrid mesh is generated for each case. At the near field, the unstructured mesh is applied, while the structured mesh is used at the far field, as shown in Fig. 2.7. The mesh of the cross section of the wind channel is shown in Fig. 2.8(a). Figure 2.8(b) shows the mesh for the rotor.

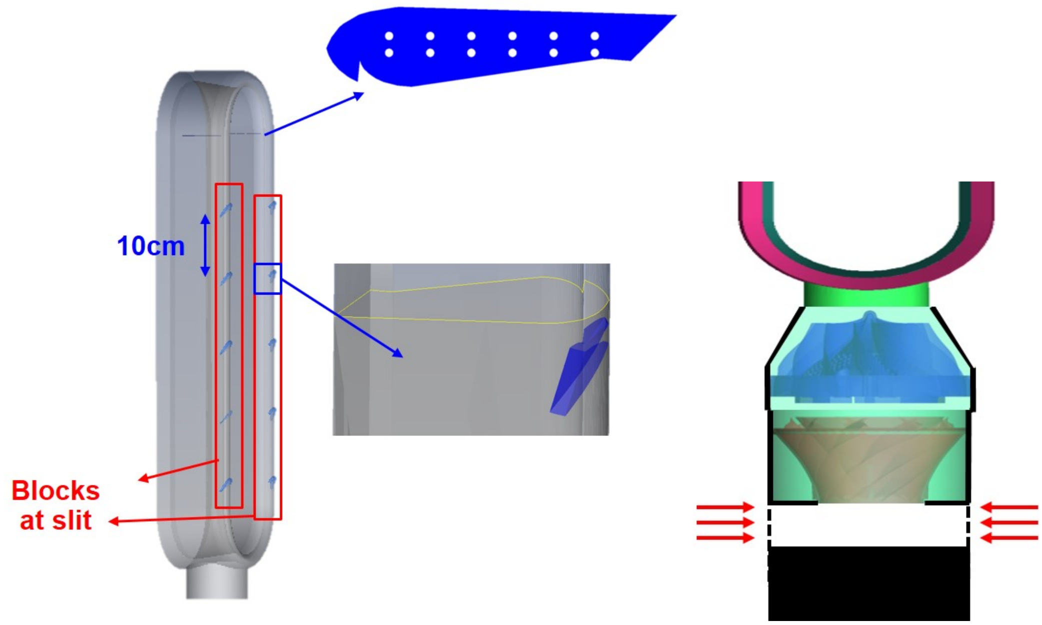

(a) (b)

Figure 2.5. Schematic of (a) the wind channel, and (b) the base.

Mesh independency test is conducted with four sets of grids, N=4,060,000; 6,320,000; 8,120,000 and 9,680,000, respectively. The streamwise velocity distribution over a reference line (centerline at x=1.5m) is plotted in Fig. 2.9. The results predicted by grids 6,320,000 do not show evident difference from those obtained by refined grids. Thus, the subsequent analysis is based on simulations using 6,320,000 grids.

2.3.1 Boundary Conditions

By measuring velocity magnitude by the hotwire anemometer at the wind channel inlet, a velocity profile is obtained, as illustrated in Fig. 2.10. r is the distance away from the center of the wind channel inlet. A fitting function is estimated as below,

$$v(r) = -1.6 \times 10^4 r^4 - 2.3 \times 10^3 r^3 + 6.5 \times 10^3 r^2 - 8.86r + 14.03 (0 \leq r \leq 0.4m)$$

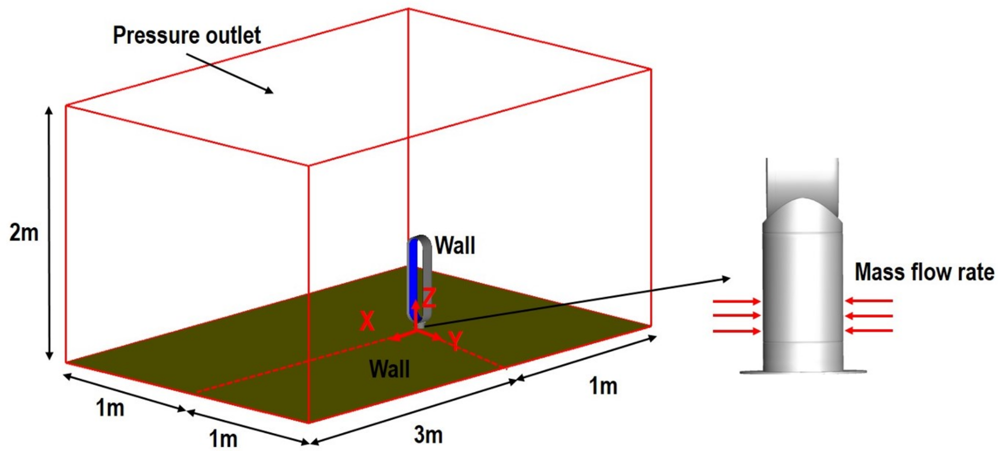

(a)

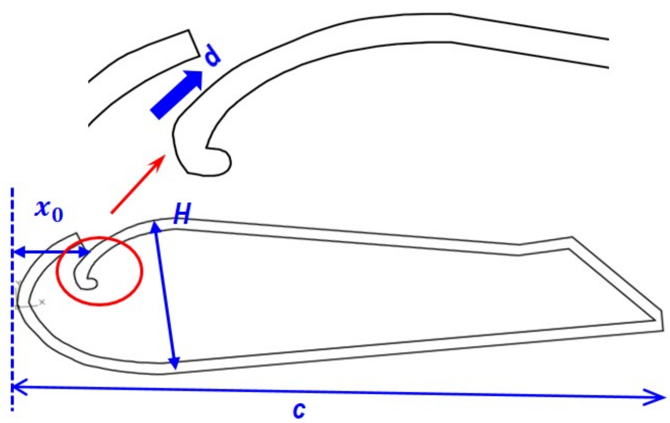

(b)

Figure 2.6. (a) Computational domain and boundary conditions. (b) The cross-section of the wind channel (d: slit width; H: cross-section height; c: chord length; x_0: slit location)

Based on the fitting function, mass flow rate at inlet is calculated, $Q_{inlet} = 0.11$kg/s. When investigating the effect of the geometric parameters of the wind channel, the inlet mass flow rate is defined as the inlet boundary condition.

In the case with rotor and stator in the base, since the rotating speed of the rotor is specified, $\omega = 8480$RPM, then pressure boundary condition, p_{inlet}=-41.56Pa, is defined at inlet, which is determined by the measurement via the manometer.

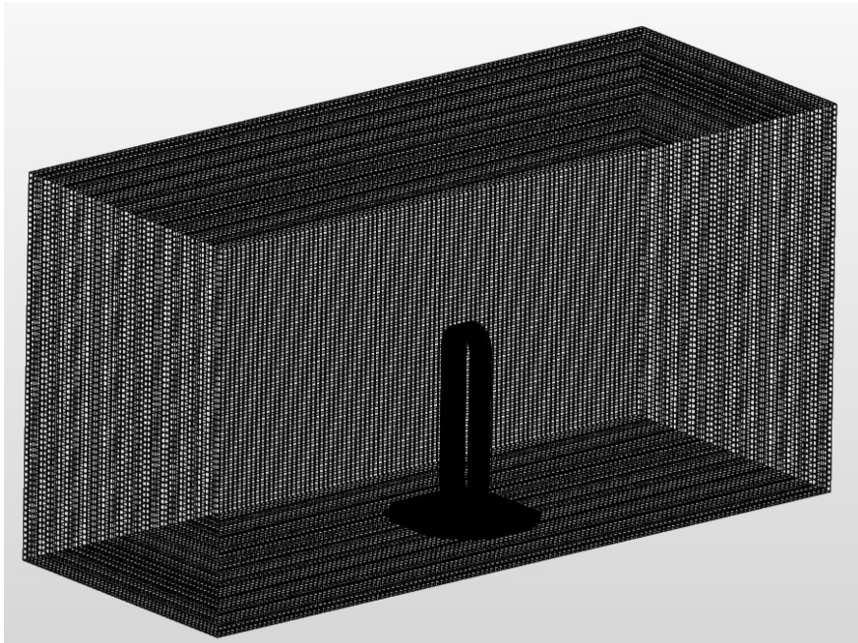

(a)

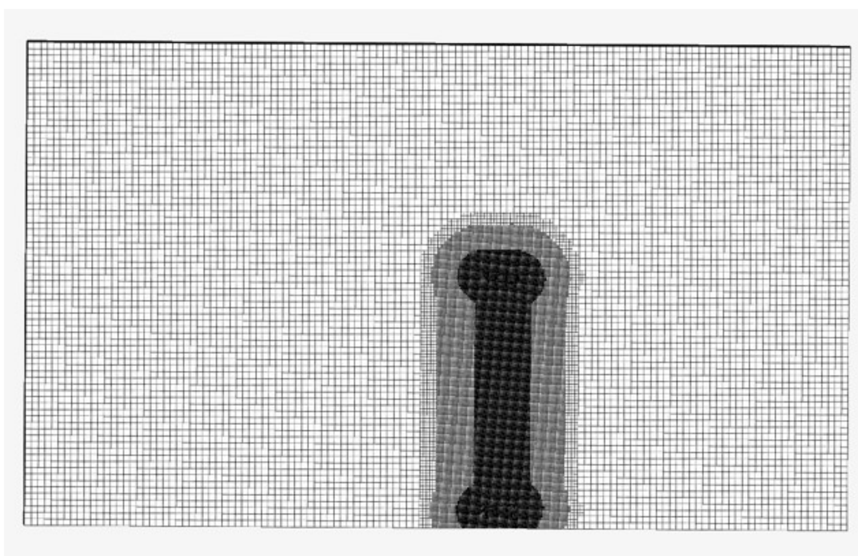

(b)

Figure 2.7. Mesh of (a) computational domain, and (b) center plane.

No-slip conditions are presented to the fan's wall and the floor of the computational domain. The side and top surfaces of the computational domain are defined as pressure outlet with zero gauge pressure.

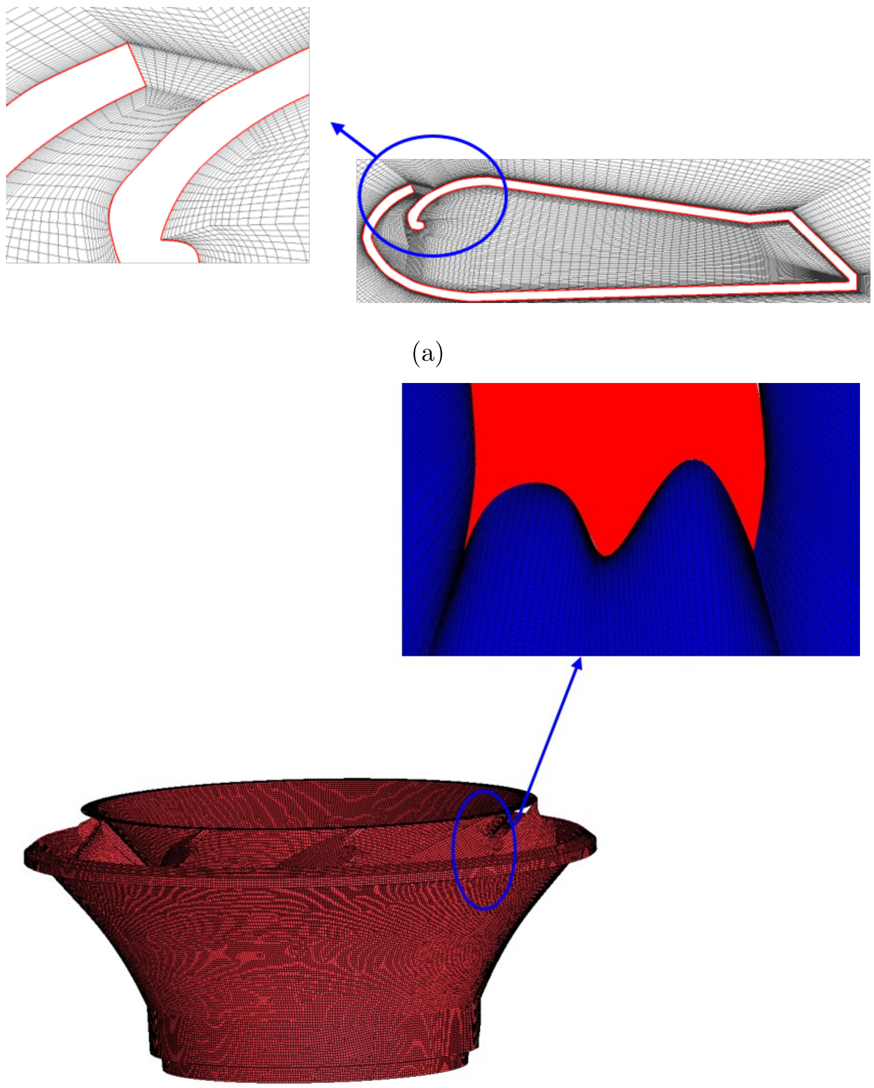

(a)

(b)

Figure 2.8. Mesh of (a) cross-section of the wind channel, and (b) the rotor.

2.3.2 Turbulence Model

There are low-speed flow regions in the flow field of the bladeless fan, in which the viscous force can not be neglected, so the viscous model is applied in the present study.

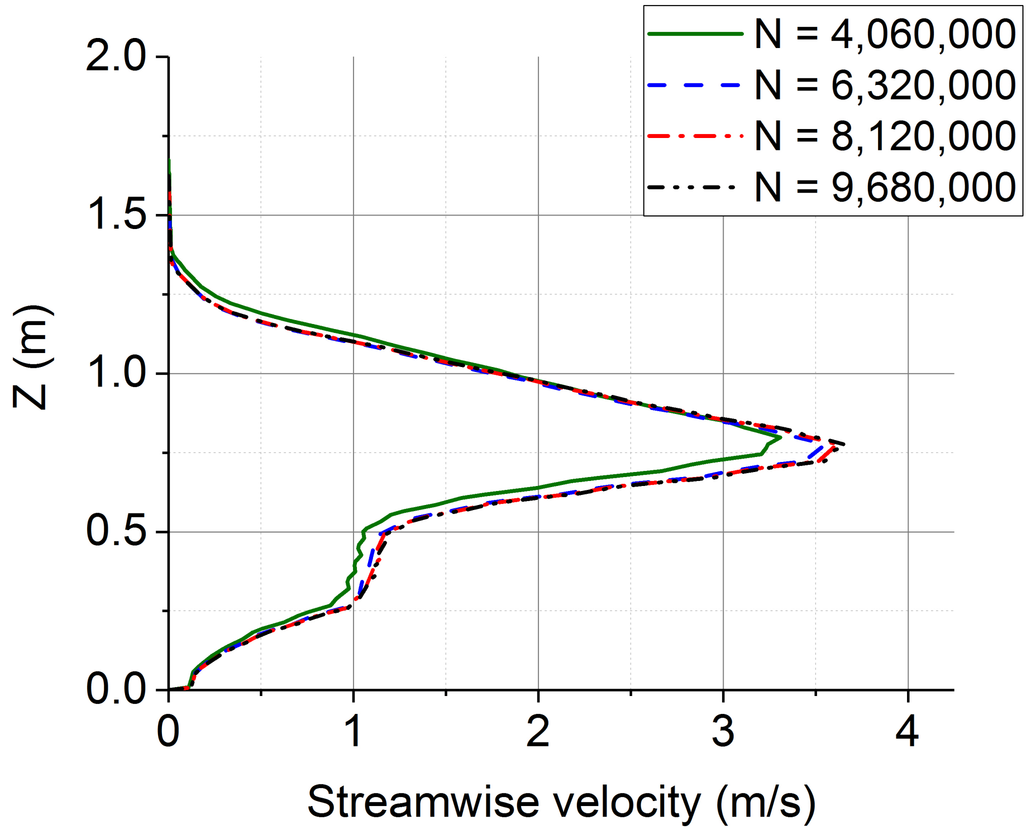

Figure 2.9. Streamwise velocity with different quantities of grids

In the flow field of the bladeless fan, there are two high-speed flow regions, which are located at the slit and the rotating rotor, respectively. At the slit, the maximum velocity is 24m/s and the temperature is 26.2°C. The corresponding Mach number is 0.07, which is less than 0.3. Thus, the flow field of the bladeless fan can be regarded as incompressible flow.

The velocity at the intake is also measured. At the intake, the mean velocity is 2.1m/s. The Reynolds number at the intake and the slit are calculated by:

$$Re = \frac{\rho u L}{\mu} \tag{2.1}$$

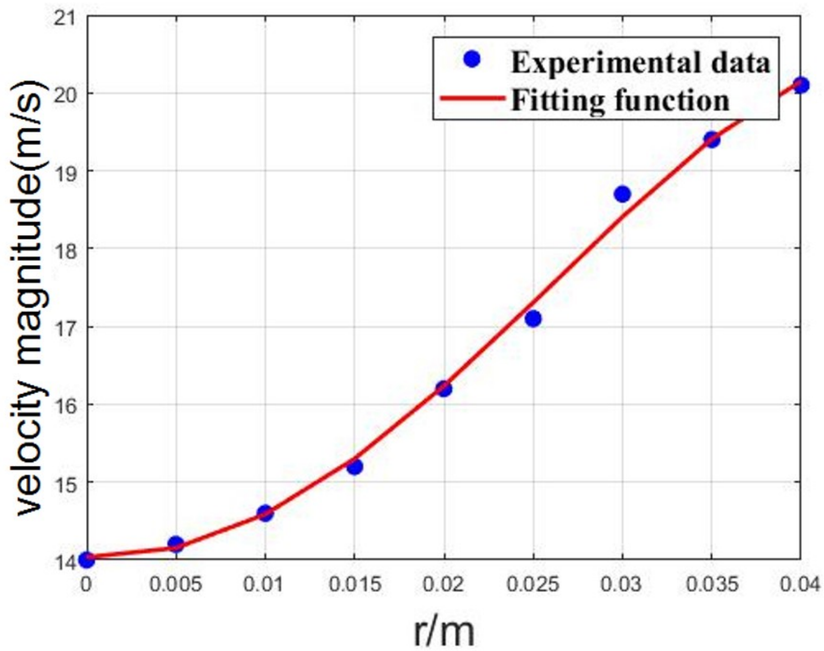

Figure 2.10. Velocity profile at the wind channel inlet

where ρ is air density, L is the characteristic length, and μ is the dynamic viscosity of the air. The density and the dynamic visocisity of the air are $1.184kg/m^3$ and $1.849\times10^{-5}kg/(m{\cdot}s)$. At the slit, the characteristic length is the slid width, d =2mm. At the intake, the characteristic length is the width of the intake, D=5cm. Therefore, the Reynolds number at the slit and the intake are 3073 and 6723. Both of them are larger than 2300, so the flow field of the bladeless fan is turbulent flow.

In the present study, $k - \epsilon$ turbulence model is applied for steady field and Smagorinsky-Lilly model is used for Large Eddy Simulation.

2.3.3 Simulation Solver Set-up

In the present study, openFoam is employed to run simulations. When studying the influence of the geometric parameters of the wind channel, SIMPLE algorithm is implemented via simpleFOAM solver in openFoam for simulations of flow through the wind channel. This solver is widely used in steady-state solution for incompressible flow (Moukalled et al., 2016). Gradient schemes of velocity and pressure are both defined as Gauss linear. As for the divergence scheme, bounded Gauss upwind is used. For each case, the steady RANS simulation is carried out first until it is converged. Then, LES is carried out with the time step of 10^{-4}s. The highest frequency investigated is 5000Hz. LES is carried out for 20s and the flow data, i.e. velocity and pressure, from 4s to 20s are exported for post-processing.

When investigating the performance of the entire fan prototype, the rotating impeller is included. Thus, an incompressible combined transient SIMPLE-PISO algorithm is applied by the pimpleDyFoam solver in openFoam. This algorithm allows to use large time step and meanwhile provide high stability (Issa, 1986). Similar to the steady state, Gauss linear is used for gradient schemes and bounded Gauss upwind is used for divergence schemes. For each case, unsteady RANS simulation with the time step of 4×10^{-5}s is carried out for 1s. The corresponding rotation angle of the rotor is 2°. After the URANS simulation is converged, LES is carried out for 15s with the time step of 4×10^{-5}s. The flow data from 5s to 15s are exported for further post-processing.

LibAcoustics in openFoam is employed to calculate the sound field around the bladeless fan. FW-H analogy is applied and Formulation 1A derived by Farassat (**?**) is used to solve FW-H equation. When investigating the aeroacoustic performance of the bladeless fan, the entire fan and the floor are defined as the noise sources. When studying the influence of the geometric parameters of the wind channel, only the wind channel of the bladeless fan and the floor are considered as the noise sources.

2.4 Investigated Geometric Parameters

In this study, the effect of four geometric parameters on performances of the bladeless fan is investigated. The first parameter is the width of slit. As shown in Fig. 2.11, the widths of the slit are 1.5mm, 2.0mm, 2.5mm and 3.0mm, respectively.

The corresponding non-dimensional width, d/c, are 1.25%, 1.67%, 2.08% and 2.50%, respectively. The airfoil profile, height of cross-section and the location of the slit are identical for all cases, the same as the one for the baseline model.

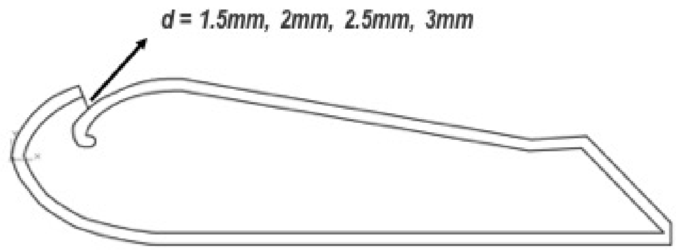

Figure 2.11. Cross-section of the wind channel with the slit width of 1.5mm, 2mm, 2.5mm and 3mm.

The second parameter is the height of cross-section. The heights of 2cm, 3cm, 4cm and 5cm are considered, as shown in Fig. 2.12, and the corresponding non-dimensional heights H/c are 16.7%, 25.0%, 33.3% and 41.7%, respectively. In these four cases, the width of slit is 2mm and the slit is located at 10% of the chord.

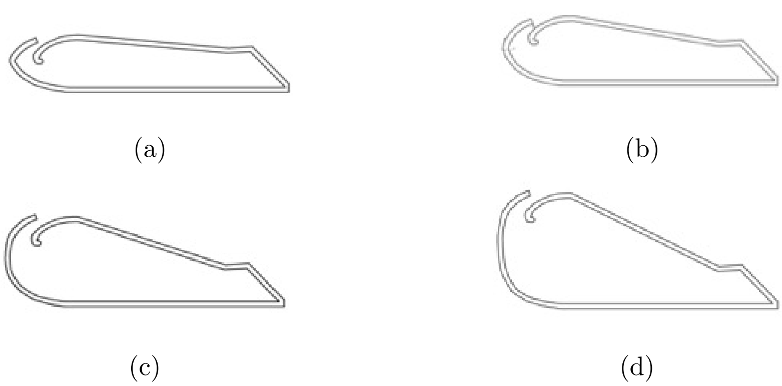

Figure 2.12. Cross-section of the wind channel with distinct heights (a) 2cm, (b) 3cm, (c) 4cm and (d) 5cm.

The effect of the slit location is also investigated. The cross-section with locations of slit of 5%, 10%, 15% and 20% of chord are designed in Fig. 2.13. The performances of airfoil profiles for the wind channel are compared to the baseline model. The three airfoil profiles, NACA0015, CLARK YM-15 and EPPLER 478, are studied. For all cases, the slit with a width of 2mm is located at 10% of chord and the height of cross-section is 3cm, as shown in Fig. 2.14.

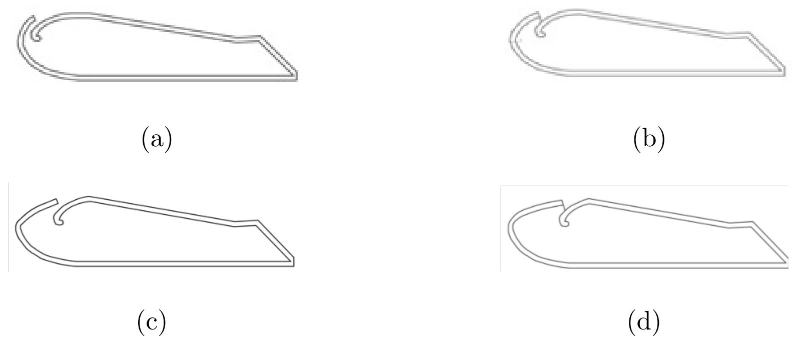

Figure 2.13. Cross-section of the wind channel with distinct locations of slit (a) $x_0/c = 5\%$, (b) $x_0/c = 10\%$, (c) $x_0/c = 15\%$ and (d) $x_0/c = 20\%$.

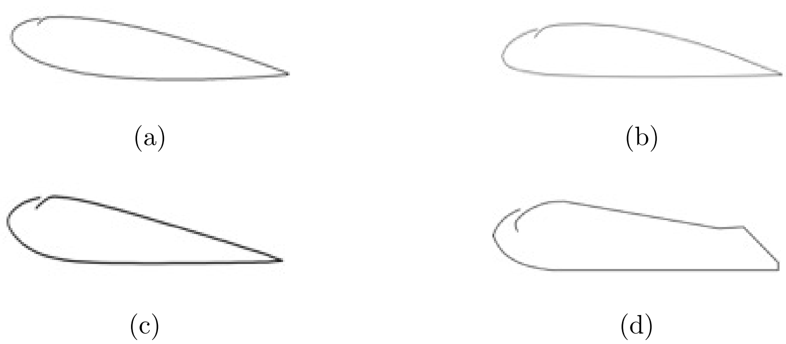

Figure 2.14. Cross-section of the wind channel with different airfoil profiles: (a) NACA0015, (b) Clark YM-15, (c) Eppler 478 and (d) Baseline.

3. VALIDATION OF SIMULATION RESULTS

3.1 Aerodynamic Result Validation

Air velocity along x direction is measured to validate the numerical simulation. The numerical results from the baseline model are compared with experimental data. Figure 3.1 illustrates x velocity contour at $x = 1.5$m. The numerical simulation is able to predict the position of the influence zone and peak velocity accurately, but the shape of the influence zone obtained by CFD and experiment are not exactly the same. In order to present the comparison further, two reference lines are defined as shown in Fig. 3.2. As illustrated in Fig. 3.3(a), the peak x velocity and the position where the peak velocity occurs obtained by CFD and experiments are in a good agreement. However, at the lower height, x velocity predicted by numerical simulations are larger than that measured in experiments and LES result is much closer to experimental results. Fig. 3.3(b) shows x velocity profile along the horizontal reference line. The numerical results match with experimental result precisely. In general, numerical method applied in the present study is able to predict aerodynamic performance of the bladeless fan accurately.

3.2 Aeroacoustic Result Validation

The sound pressure level at near field and far field are calculated from the LES results. Figure 3.4 shows two defined receivers. Both of them are located at $z = 0.8$m, and the distance from the bladeless fan is 0.1m and 1.5m.

Figure 3.5(a) illustrates the sound pressure level at near field obtained by numerical simulations and experiments. At all frequencies, sound pressure level calculated by numerical method is lower than that measured in experiments, especially between

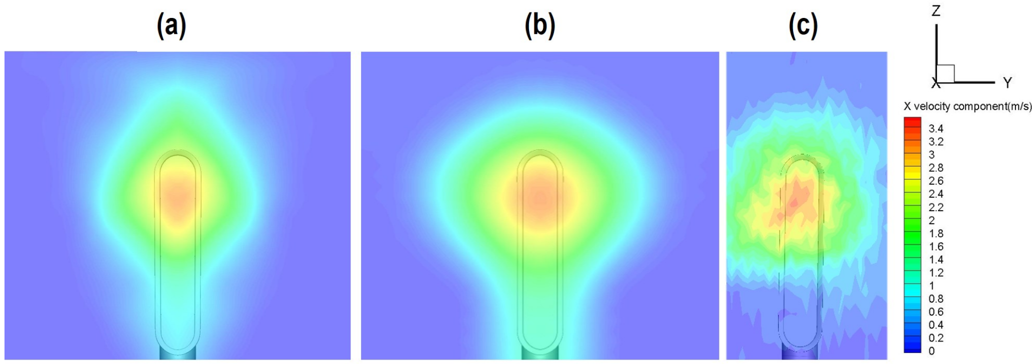

Figure 3.1. X velocity contour at x = 1.5m obtained by: (a) LES (averaged from t=5s to 15s), (b) RANS, (c) experiment

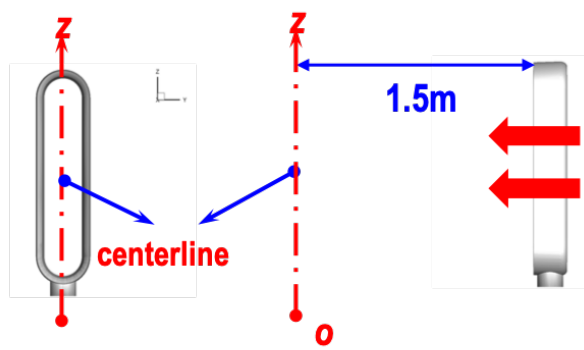

(a)

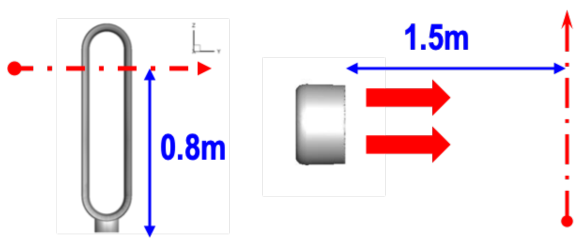

(b)

Figure 3.2. (a) Reference line along vertical direction. (b) Reference line along horizontal direction

3800Hz and 5000Hz. Since structure vibration is not considered in simulations, then mechanical noise generated by the vibration is not included in numerical results. In

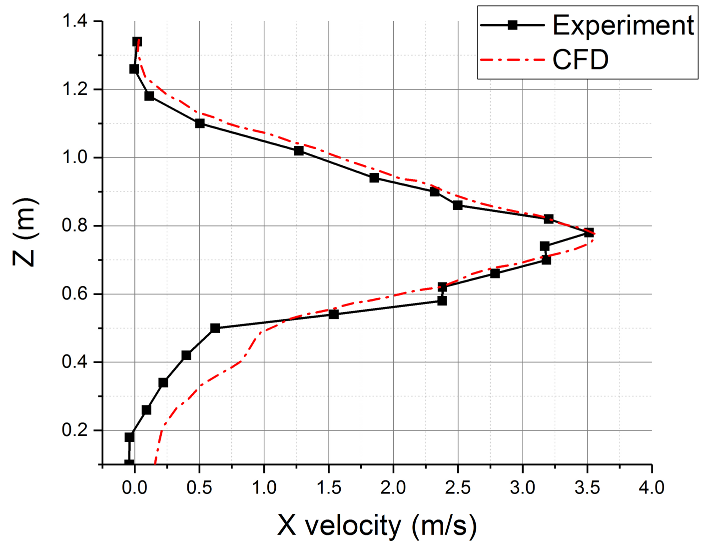

(a)

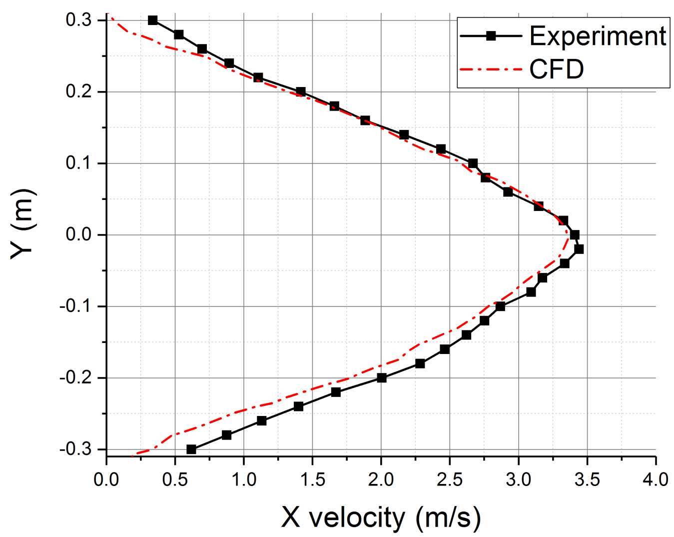

(b)

Figure 3.3. (a) Velocity distribution along the horizontal reference line. (b) Velocity distribution along the vertical reference line.

this case, the rotating speed of the rotor is 8480rpm, so the corresponding blade passage frequency is 1272Hz. In numerical result, a signature peak can be observed at 1252Hz. Thus, the blade passage frequency is able to be predicted by Ffowcs Williams and Hawkings model at near field.

At far field, as shown in Fig. 3.5(b), sound pressure level predicted by Ffowcs Williams and Hawkings model is still lower than experimental data and the difference is approximately 5dB at lower frequencies. It is caused by the lack of noise generated by mechanical vibration in simulations.

In general, the difference between the numerical and experimental results is acceptable.

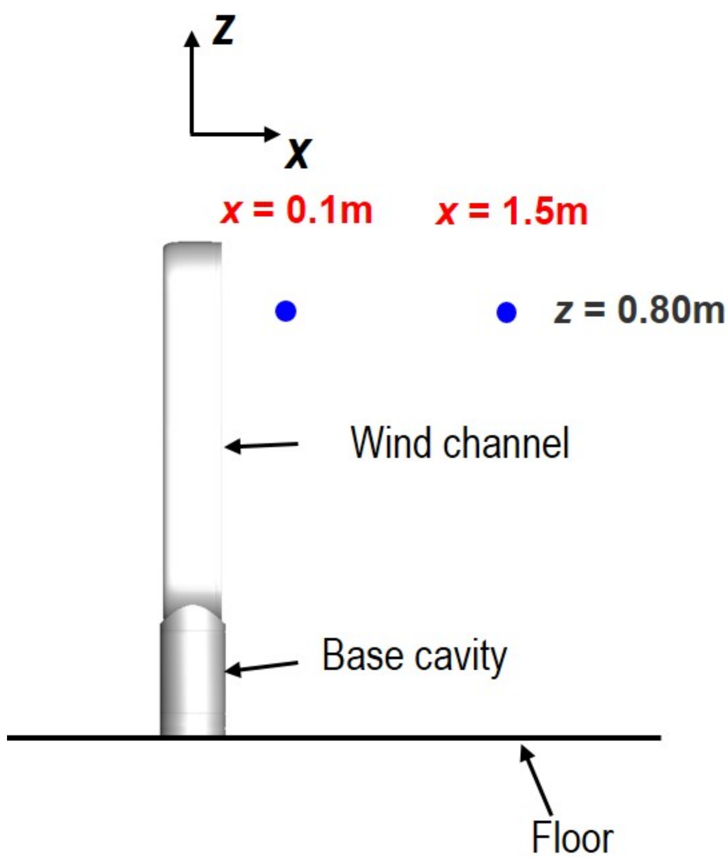

Figure 3.4. Two receivers at near field and far field

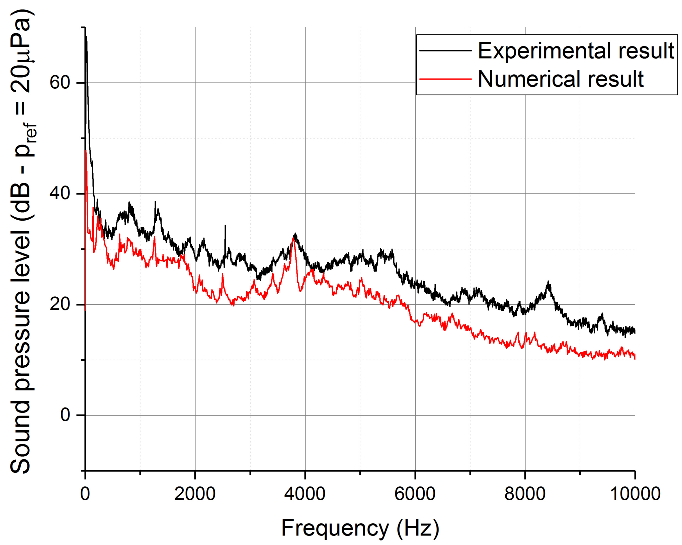

(a)

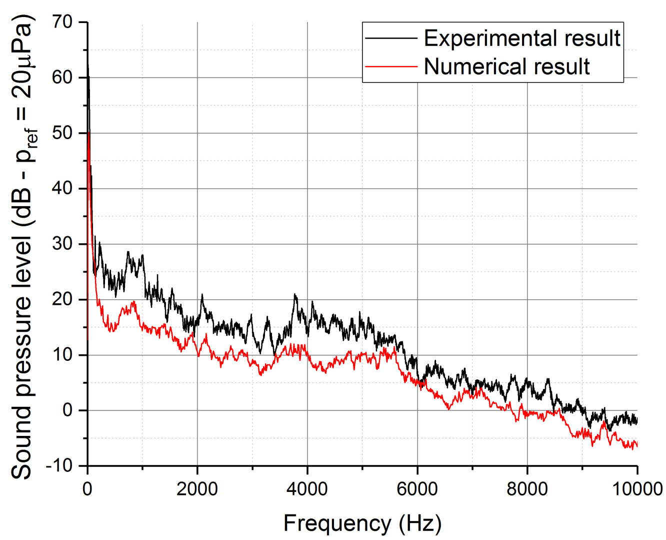

(b)

Figure 3.5. (a) Sound pressure level at near field. (b) Sound pressure level at far field.

4. AERODYNAMIC PERFORMANCE

4.1 Flow Characteristic

To characterize the aerodynamic performance of the bladeless fan, averaged flow data is calculated by LES results from the flow time of 4s to 15s. Three height levels are selected to investigate the development of the flow outside the bladeless fan, including $z = 0.3$m, $z = 0.55$m, $z = 0.8$m, as shown in Fig. 4.1. $z = 0.3$m corresponds to the height of the bottom of the wind channel, and $z = 0.8$m corresponds to the location of the beginning of the arch part of the wind channel. Mean x velocity contours over these three planes are generated, as shown in Fig. 4.2.

Figure 4.1. Planes at $z = 0.3$m, $z = 0.55$m and $z = 0.8$m

Fig. 4.2(a) illustrates that there is a hotspot at the center of the wind channel. With the increase of the height, the flow at near field is divided into two jets and x velocity becomes lower. However, the region of the influence zone becomes larger, as shown in Fig. 4.2(b) and Fig. 4.2(c).

To investigate the flow structure outside the bladeless fan, streamlines around the baseline model are plotted using averaged velocity. As shown in Fig. 4.3(a), the outflow at far field of the bladeless fan consists of the air blown out from the slit of the wind channel and entrained from the back and side of the fan. Figure 4.3(b)

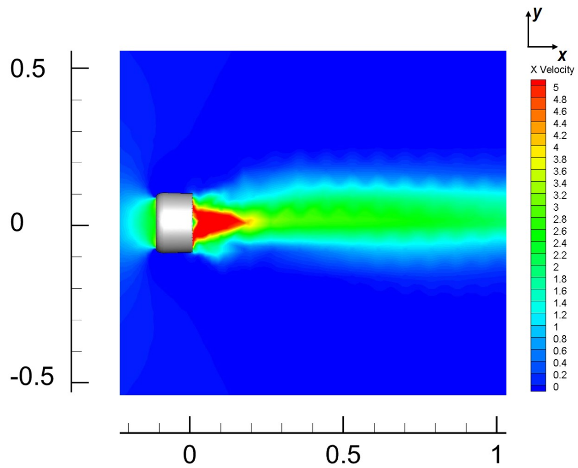

(a)

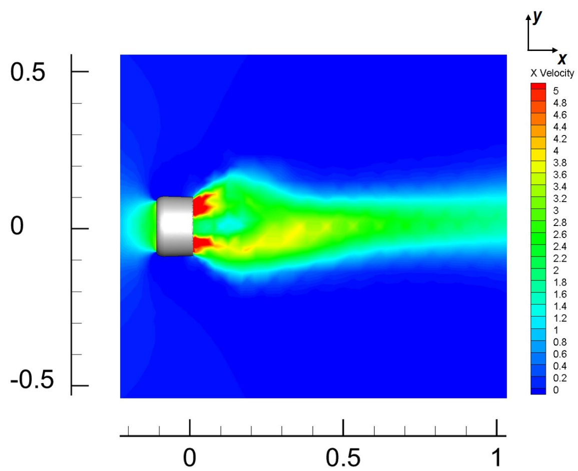

(b)

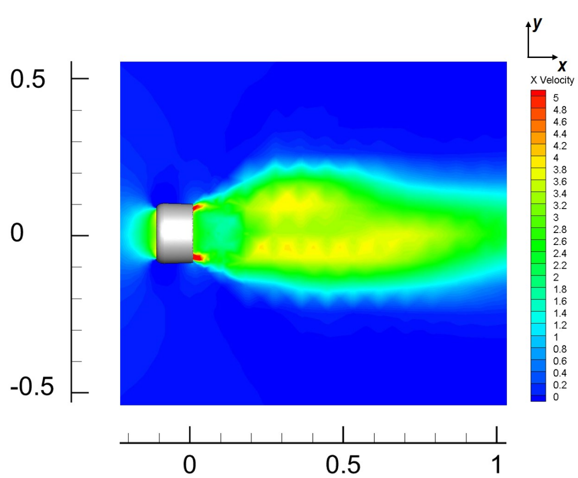

(c)

Figure 4.2. X velocity contours at (a) $z = 0.3$m, (b) $z = 0.55$m, and (c) $z = 0.8$m

illustrates the flow direction. As the air goes away from the fan, it moves upwards simultaneously.

Furthermore, velocity profiles on both the horizontal and vertical directions at different distances away from the bladeless fan are illustrated. Figure 4.4(a) shows the velocity profiles on horizontal direction at height $z = 0.8$m. It is found at the near field, $x = 0.1$m, the flow is formed by two jets. As far away from the fan, the two jets start to merge, forming a flow similar to a single jet at $x = 0.5$m.

Velocity distribution along the vertical direction is shown in Fig. 4.4(b). At near field, there are two separated jets at the top and the bottom of the annular wind channel. As the distance away from the fan increases, similar to the velocity profile along horizontal direction, the two jets merge and form a single jet. At far field, the velocity at lower height is very low, forming a low energy region. It agrees with the results reported in (Li et al., 2016).

4.2 Influence of the Geometric Parameters of the Wind Channel

To illustrate the influence of the geometric parameters on the performances of the bladeless fan, several reference planes are defined, as shown in Fig. 4.5. Reference plane 1 is the central XZ plane $y = 0$m). Reference plane 2 is a XY plane ($z = 0.8$m). Reference plane 3 and 4 are two YZ plane ($x = 1.5$m and -0.5m, respectively). Streamwise averaged velocity, u_x, at $x = 1.5$m is used to evaluate aerodynamic performance. Non-dimensional velocity, u_x/u_{inlet}, is calculated, where u_{inlet} is the mean velocity at inlet ($u_{inlet} = 2.5$m/s). In addition, mass flow rates at inlet, Q_{inlet}, and the reference planes located at reference plane 3 and reference plane 4, Q_{back} and Q_{total}, are estimated. Then, the ratios of mass flow rate are defined by

$$M_1 = \frac{Q_{total}}{Q_{inlet}}, \tag{4.1}$$

and

$$M_2 = \frac{Q_{back}}{Q_{inlet}}. \tag{4.2}$$

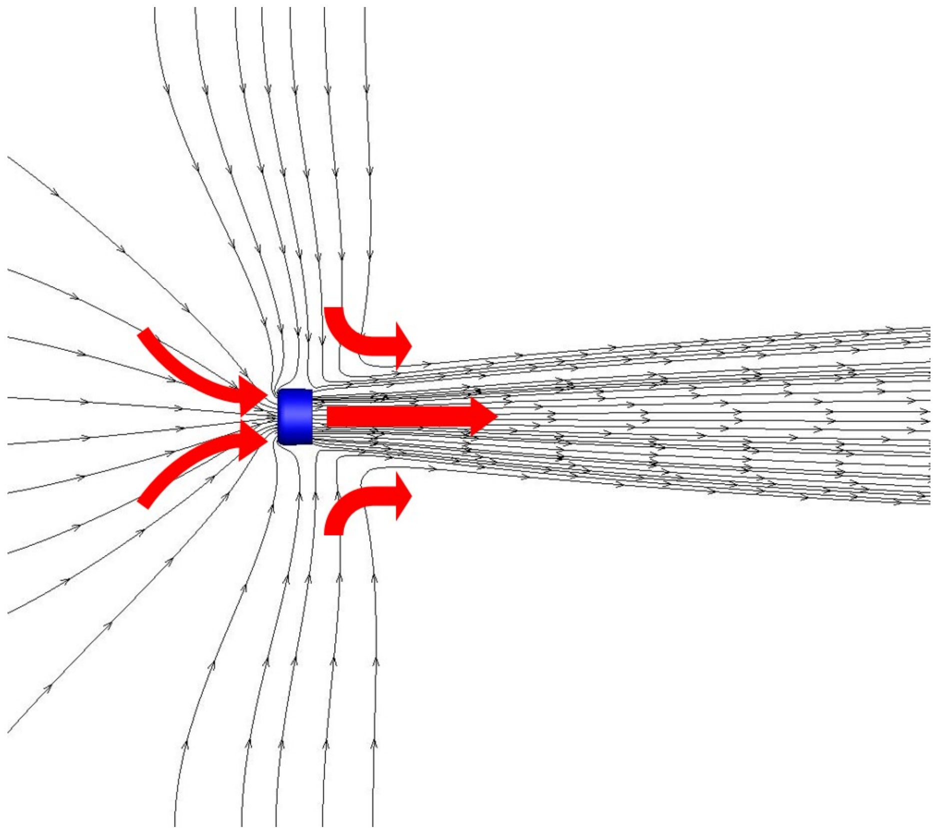

(a)

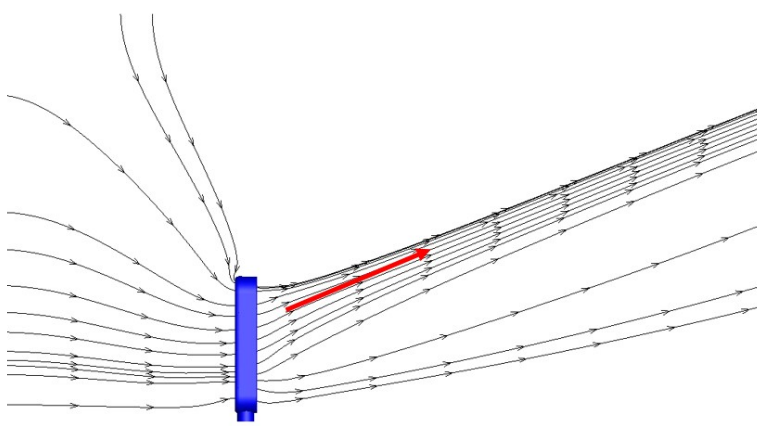

(b)

Figure 4.3. Streamline of the averaged flow field (a) over horizontal plane ($z = 0.8$m) and (b) in the central vertical plane ($y = 0$m)

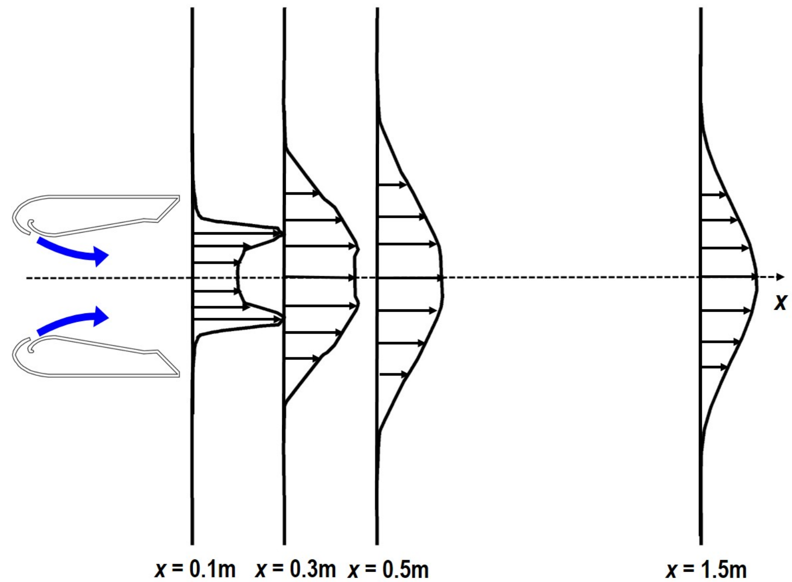

(a)

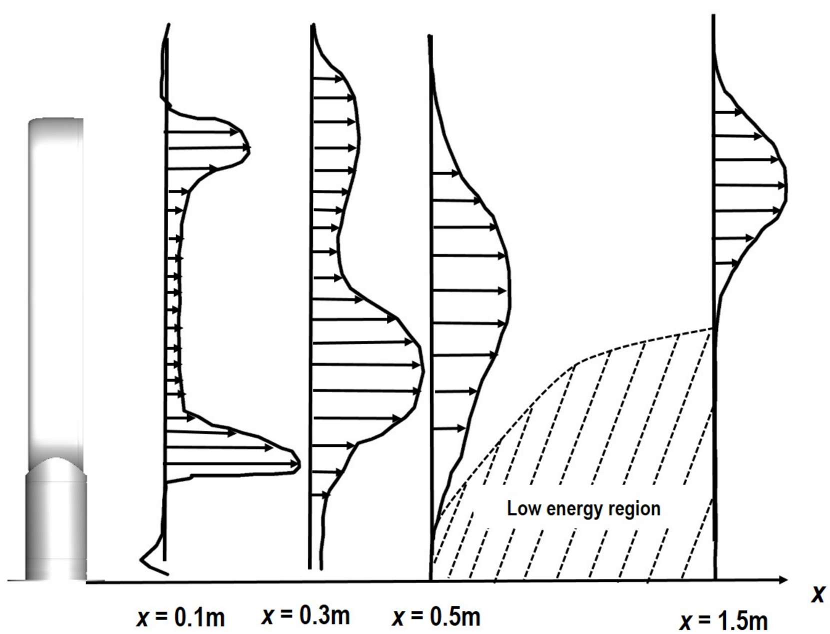

(b)

Figure 4.4. Profiles of the averaged velocity (x component) at different downstream location (a) over horizontal plane ($z = 0.8$m) and (b) in the central vertical plane ($y = 0$m)

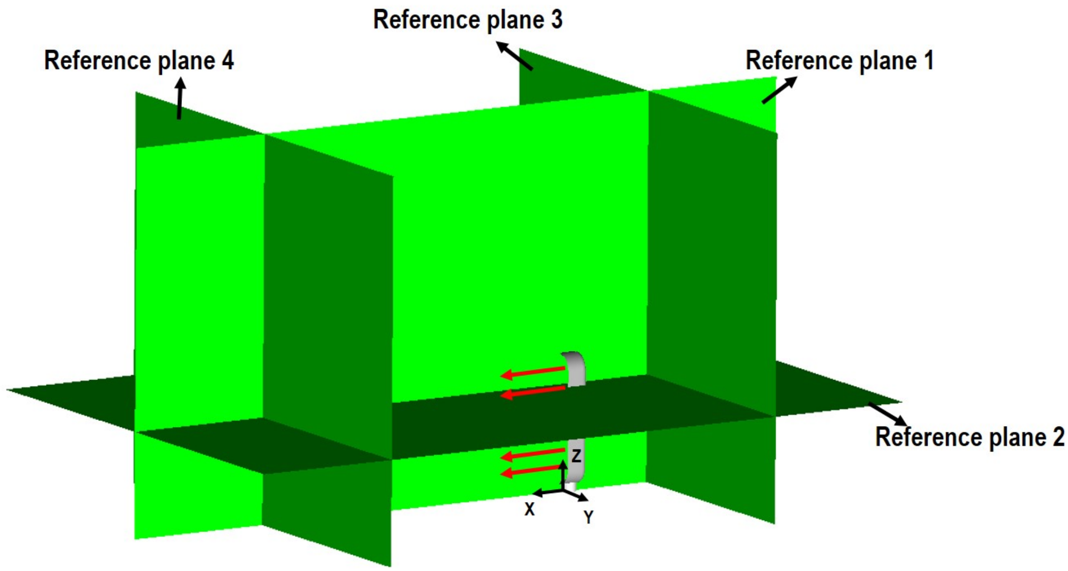

Figure 4.5. Schematic of the reference planes

4.2.1 Effect of the Slit Width

The first investigated parameter is the width of slit. The mean x velocity contours at $x = 1.5$m with different slit width are illustrated in Fig. 4.6. It is shown that with the decrease of the slit width, the height of the influence zone becomes lower. For the bladeless fan with slit width of 3mm ($d/c = 2.5\%$), the center of influence zone is located at $z = 1.1$m, which is higher than the fan, while for the bladeless fan with slit width of 1.5mm ($d/c = 1.25\%$), the center of the influence zone moves downwards to $z = 0.6$m, which is close to the center of the wind channel, more suitable for household appliances. Furthermore, by narrowing the width of slit, u_x increases. The velocity profiles at different distances away from the bladeless fan is illustrated in Fig. 4.7. The flow structure for each case are similar. At near field of the fan, the flow is formed by two jets. As far away from the fan, the two jets start to merge, forming a flow similar to a single jet-flow. In addition, at $x = 1.5$m, with the decrease of slit width, both the peak value of x velocity and the range of influence region increase. Figure 4.8 presents the ratio of mass flow rate against the slit width. With the decrease of

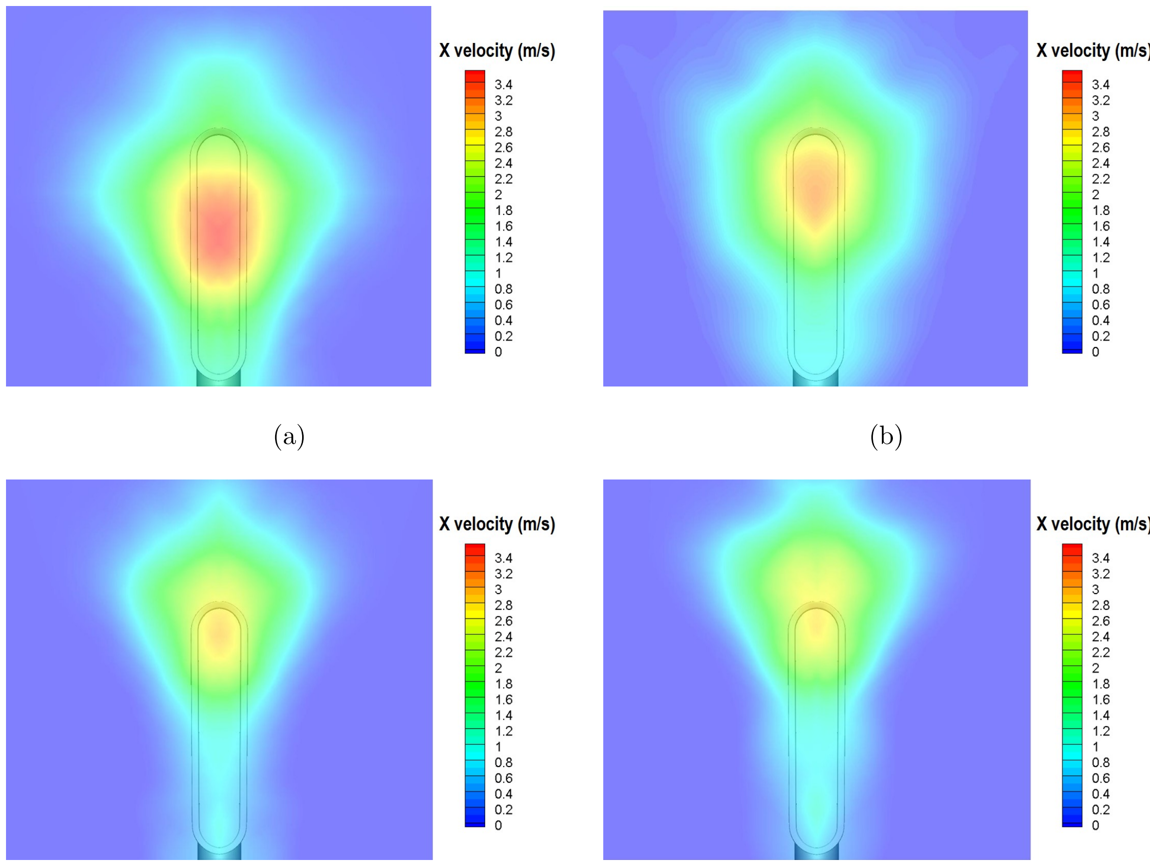

(a) (b)

(c) (d)

Figure 4.6. Mean x velocity contour at $x = 1.5$m (a) $d/c = 1.25\%$, (b) $d/c = 1.67\%$, (c) $d/c = 2.08\%$ and (d) $d/c = 2.50\%$.

the width, the ratio of mass flow rate becomes larger. In the case of the narrower slit, the outflow velocity is larger and greater pressure gradient is produced, so more air is entrained from back and side. Moreover, for all cases, M_1 is always much larger than M_2, suggesting the main increase of mass flow rate is due to the entrainment from side instead of from back.

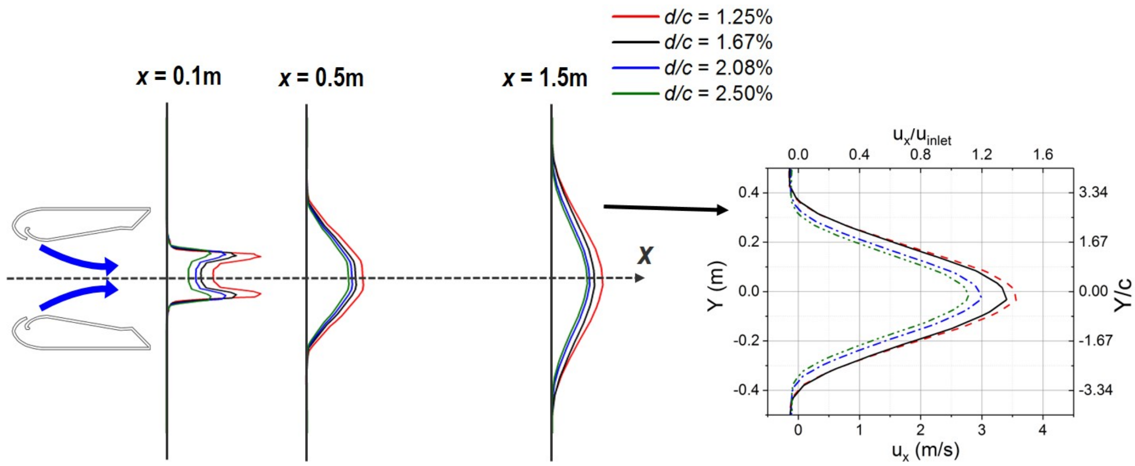

Figure 4.7. Velocity profile along horizontal direction with different slit widths

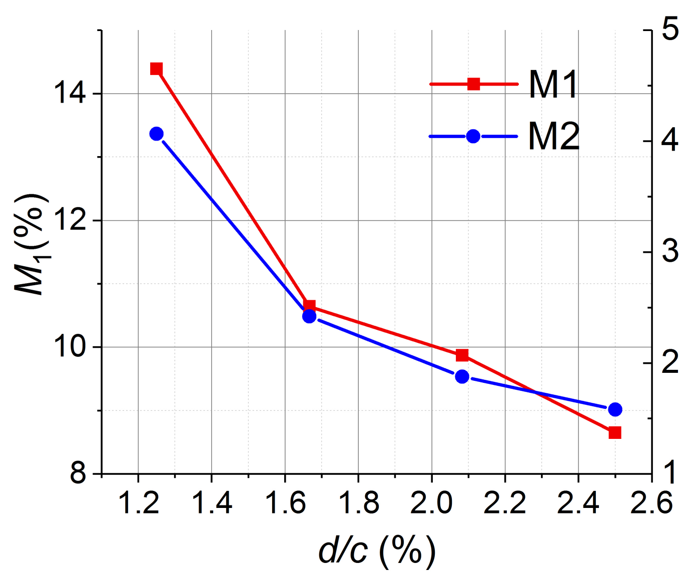

Figure 4.8. Ratio of mass flow rate for different slit widths

4.2.2 Effect of the Cross-sectional Height

The effect of the height of the cross-section is also studied. By changing the height of cross-section, the curvature of wind channel surface is changed, which influences the Coanda effect. Thus, the aerodynamic performance of the bladeless fan will be affected. X velocity contours for different height of cross-section are illustrated in Fig. 4.9. The shape of the velocity contour predicted by the cross-sectional height of $H/c = 16.7\%$ is totally different from the other three cases. Furthermore, X velocity at far field of this case is smaller than the cases with thicker cross-section. Mean x velocity profiles along the reference lines are indicated in Fig. 4.10, showing similar flow structures. At $x = 1.5$m, the case with $H/c = 33.3\%$ has the largest maximum x velocity and the widest influence zone. The ratio of mass flow rate is also calculated, shown in Fig. 4.11. The wind channel with $H/c = 33.3\%$ yields the largest ratio of mass flow rate. The possible reason is that for the thinner cross-section, the upper surface is so flat that the Coanda effect, which requires a convex surface near the jet, is not evident. However, for the cross-section with too large height, the air entrained from back is blocked. Thus, $H/c = 33.3\%$ has the best aerodynamic performance.

4.2.3 Effect of the Slit Location

The effect of the slit location on performances is also studied. Figure 4.12 illustrates the shape of the influence zone obtained by x_0/c=5% is totally different from the ones of other three. In this case, the slit is very close to the leading edge, the angle between the direction of jet flow and the streamwise direction is large, and the jet is far away from the convex surface so that the Coanda effect is not significant. As shown in Fig. 4.13, at far field, the influence zone of $x_0/c = 5\%$ is wider than other cases, but the peak value of x velocity is much lower. As the slit moves closer to the location of the airfoil maximum thickness, ratios of mass flow rate increase, as shown in Fig.4.14, due to the enhanced Coanda effect.

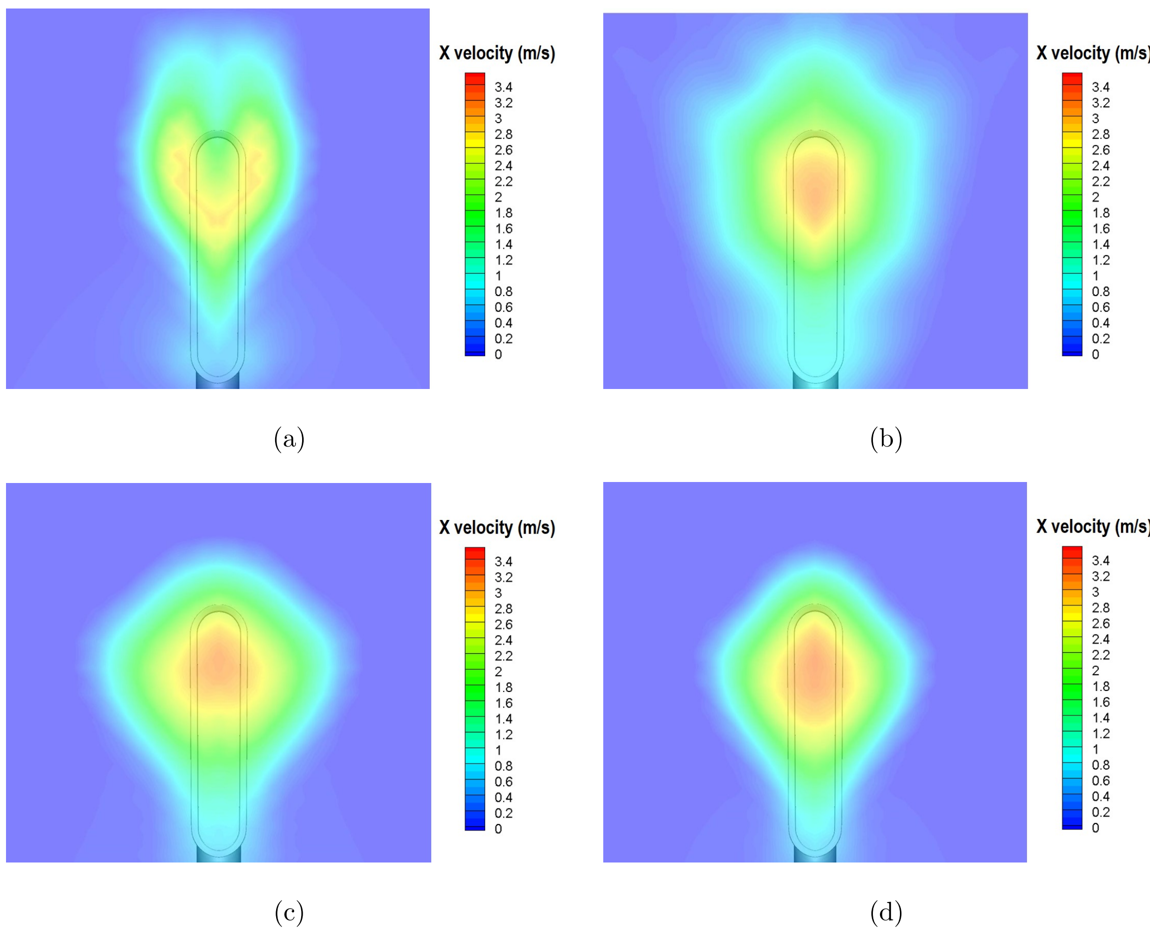

Figure 4.9. Mean x velocity contour at $x = 1.5$m (a) $H/c = 16.7\%$, (b) $H/c = 25.0\%$, (c) $H/c = 33.3\%$ and (d) $H/c = 41.7\%$.

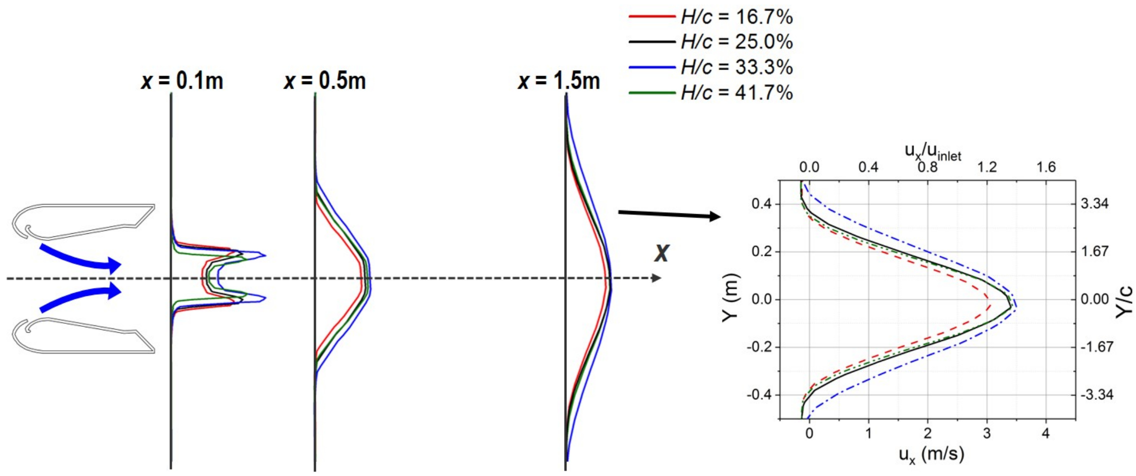

Figure 4.10. Velocity profile along horizontal direction with different cross-sectional height

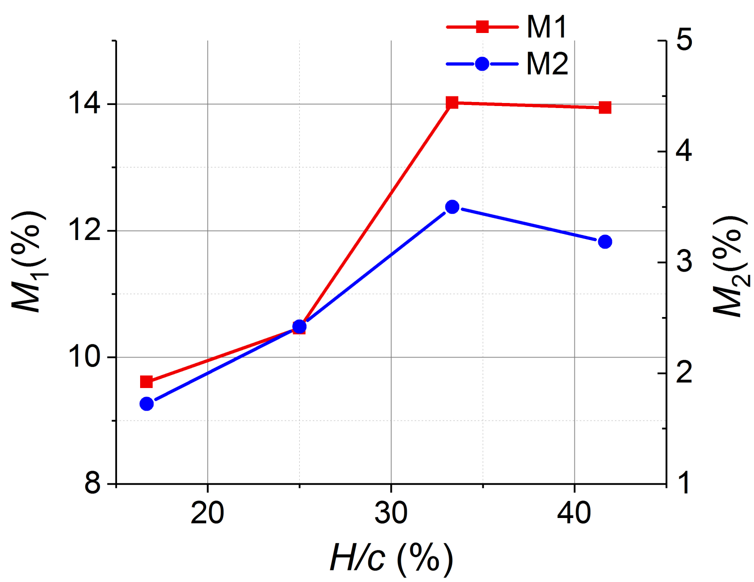

Figure 4.11. Ratio of mass flow rate for different cross-sectional height

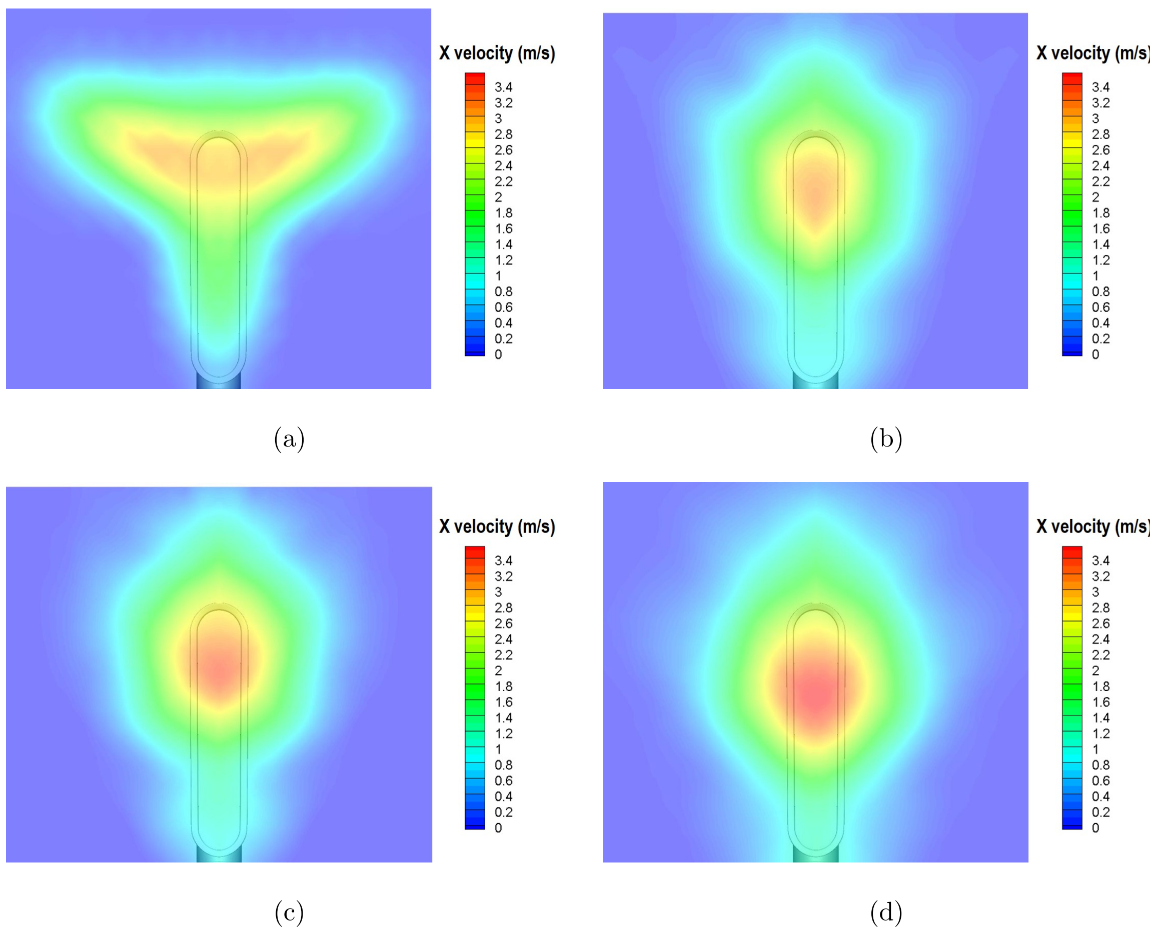

Figure 4.12. Mean x velocity contour at $x = 1.5$m (a) $x_0/c = 5\%$, (b) $x_0/c = 10\%$, (c) $x_0/c = 15\%$ and (d) $x_0/c = 20\%$.

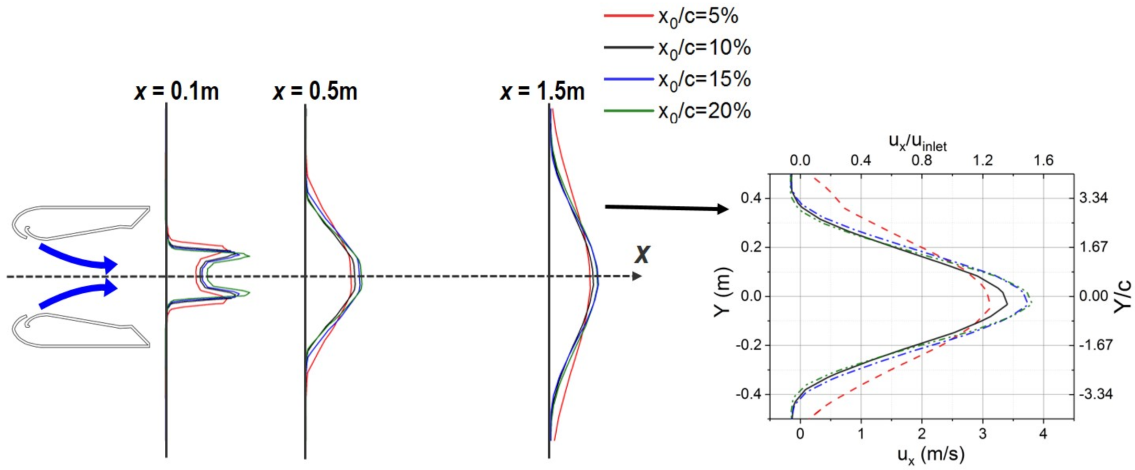

Figure 4.13. Velocity profile along horizontal direction with different locations of the slit

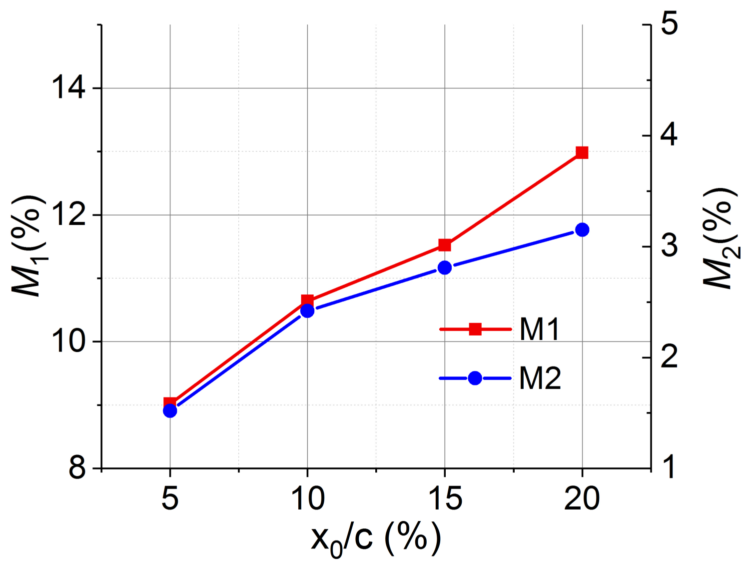

Figure 4.14. Ratio of mass flow rate for different locations of the slit

4.2.4 Effect of the Profile of the Cross-section

Figure 4.15 shows mean x velocity contours for different cross-sectional profiles. Although the maximum x velocity obtained by the cross-sectional profile of CLARK

YM-15 is the largest, the area of the influence zone is smallest. For a household fan, this feature may cause discomfort for users. For other three cases, the shape and the region of the influence zone are similar, and the x velocity obtained by EPPLER 478 is largest. Figure 4.16 illustrates streamwise velocity profile obtained by the bladeless fans with different airfoil profiles of wind channel cross-section. It shows similar phenomenon observed from velocity contours. The fan with the cross-sectional profile of CLARK YM-15 has the largest peak velocity and smallest influence zone. It indicates that the flow field produced by this case is not uniform. For the other cases, the velocity profiles are similar while EPPLER 478 gives the largest maximum streamwise velocity. However, compared to other geometric parameters, changing airfoil profile of cross-section has less impact on aerodynamic performance of the bladeless fan, because the ratios of the mass flow rate obtained by different profiles of cross-section do not change significantly (Fig. 4.17).

4.3 Summary

In this chapter, using the LES results, aerodynamic performance of the bladeless fan is characterized and the effect of the wind channel's geometric parameters is studied. The investigated geometric parameters include the slit width, the height of the cross-section, the location of the slit and the profile of the cross-section. X velocity contours, velocity profile and streamlines are used to characterize the aerodynamic performance of the bladeless fan. The main discoveries include:

i) With the increase of the height, the wind outside the fan becomes less powerful, but the region of the influence zone becomes larger.

ii) The flow outside the bladeless fan consists of the air blown out from the wind channel and entrained from the back and side of the fan. As the air moves away from the fan, it moves upwards at the same time.

iii) From the horizontal view, the flow near the bladeless fan are formed by two separated jets. The two jets merge to a single jet along the downstream direction.

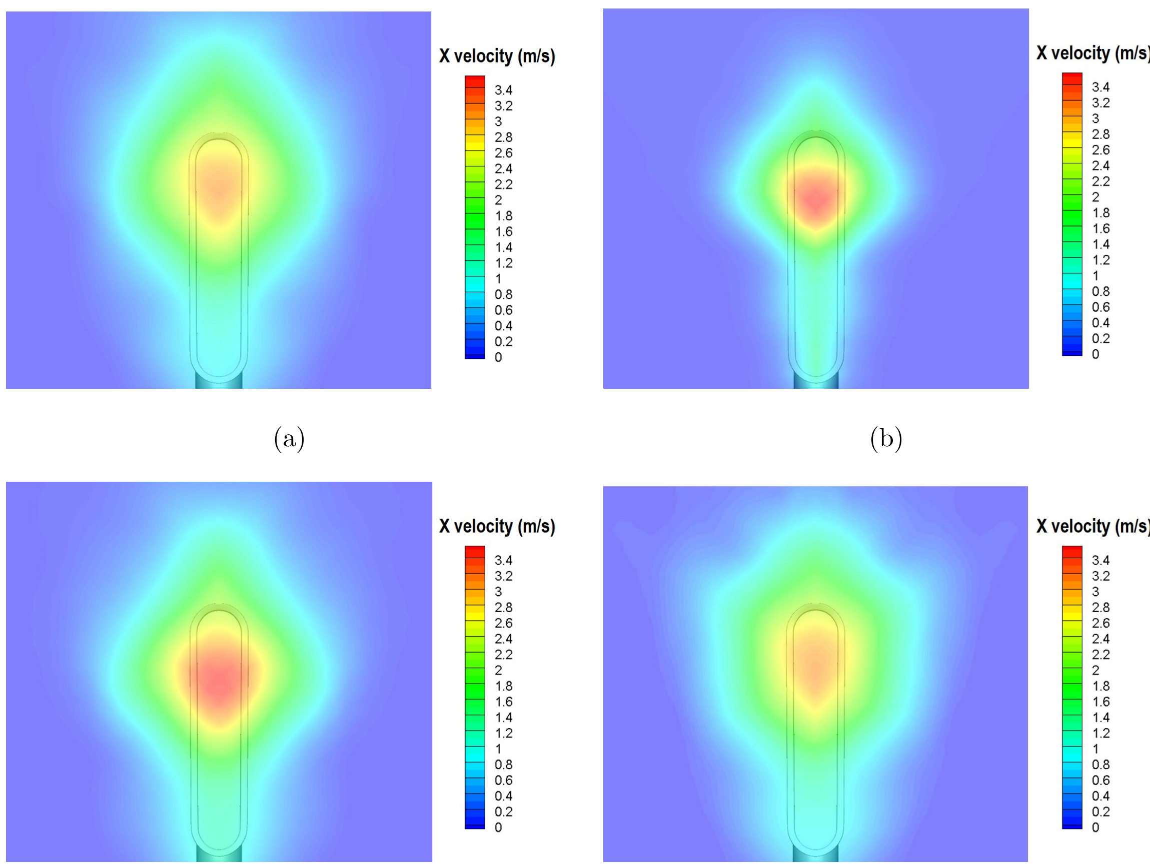

(a) (b)

(c) (d)

Figure 4.15. Mean x velocity contour at x = 1.5m (a) NACA 0015, (b) Clark YM-15, (c) EPPLER 478 and (d) Baseline.

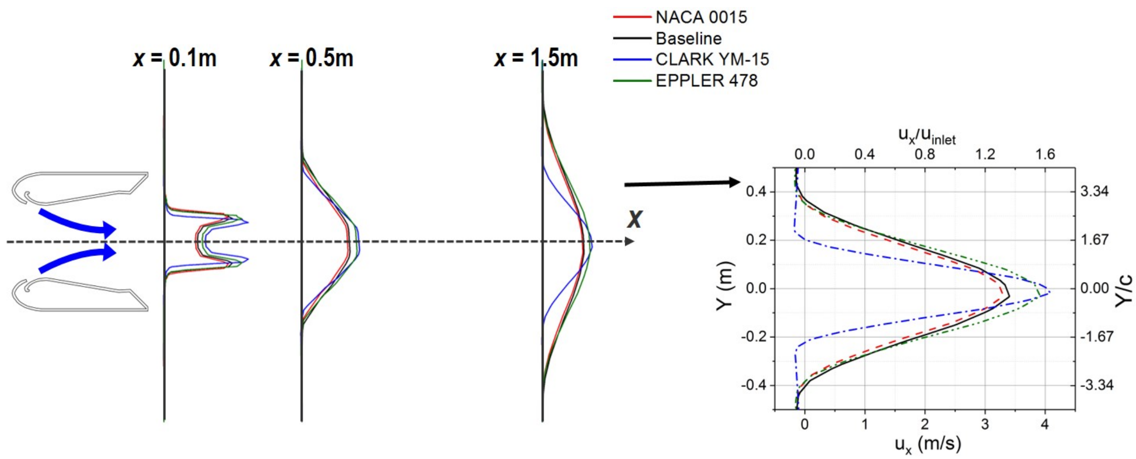

Figure 4.16. Velocity profile along horizontal direction with different profiles of the cross-section

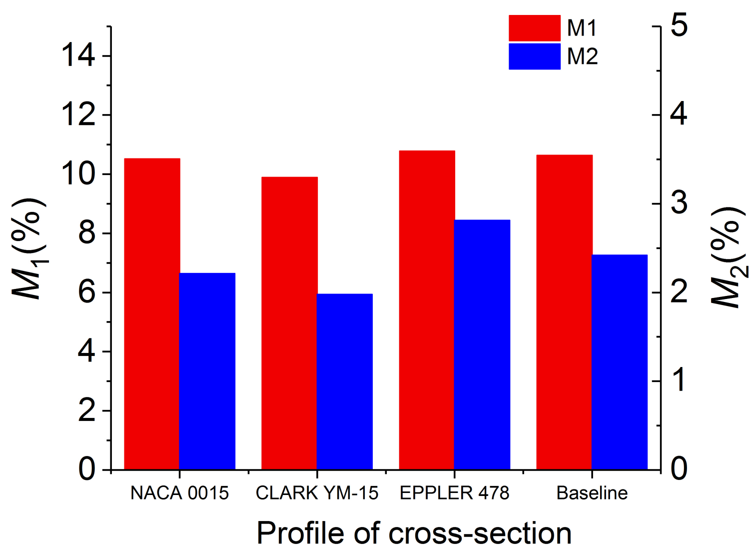

Figure 4.17. Ratio of mass flow rate for different profiles of the cross-section

iv) From the vertical view, at near field, two jets are located near the slit. As the distance away from the fan increases, the two jets merge to a single one. And at the far field, there is a low energy region at the lower height.

v) The results for slit width of 1.5mm, 2mm, 2.5mm, and 3mm, indicate that with the decrease of the slit width, both mean x velocity and the ratio of mass flow rate increase.

vi) The results for the height of cross-section of 2cm, 3cm, 4cm, and 5cm, shows that the bladeless fan with the height of cross-section of 4cm has optimal aerodynamic performance.

vii) As the slit moves closer to the location of the maximum airfoil thickness, aerodynamic performance of the bladeless fan is improved.

viii) The wind channel with the cross-sectional profile of Eppler 478 has the best aerodynamic performance. Aeroacoustic performances of the fan with different cross-sectional profile are similar. Comparing to other geometric parameters, the profile of cross-section has insignificant influence on aerodynamic performance of the bladeless fan.

5. AEROACOUSTIC PERFORMANCE

In the present study, sound pressure level is used to evaluate the aeroacoustic performance of the bladeless fan. Pressure fluctuation in the time domain, $p(t)$, is obtained from LES results. The power spectral density of sound pressure, $|p(f)|$, is calculated by Fast Fourier Transform. The sound pressure level is calculated by

$$SPL = 10 \log \left(\frac{|p(f)|}{p_{ref}} \right)^2 \tag{5.1}$$

where $p_{ref} = 20\mu\text{Pa}$. In some results shown below, A-weighting is applied. The function of A-weighting, $A(f)$ is,

$$A(f) = \frac{12194^2 \cdot f^4}{(f^2 + 20.6^2)(f^2 + 12104^2)\sqrt{f_1^2 + 107.7^2}(f^2 + 737.9^2)} \tag{5.2}$$

5.1 Aeroacoustic Characteristic of the Bladeless Fan

5.1.1 Noise Source Analysis

To find the predominant noise source, a noise source analysis is conducted. The definition of the noise sources and the receivers are shown in Fig. 5.1. The receiver at near field is located at $x = 0.1$m, $y = 0$m, $z = 0.8$m. The receiver at far field is located at $x = 1.5$m, $y = 0$m, $z = 0.8$m. Four possible noise sources are investigated, including the wind channel, the base cavity, the rotor and stator inside the base and the floor.

Figure 5.2(a) illustrates the contribution sound pressure level from different parts at near field. It is indicated that the noise produced by rotor and stator is predominant. The wind channel is the second main source and the noise generated by the floor is lowest. As for the noise at far field, as shown in Fig. 5.2(b), the rotor, stator and the wind channel are still two dominated noise sources. However, the noise produced by the base cavity decreases significantly, even lower than that generated by the floor.

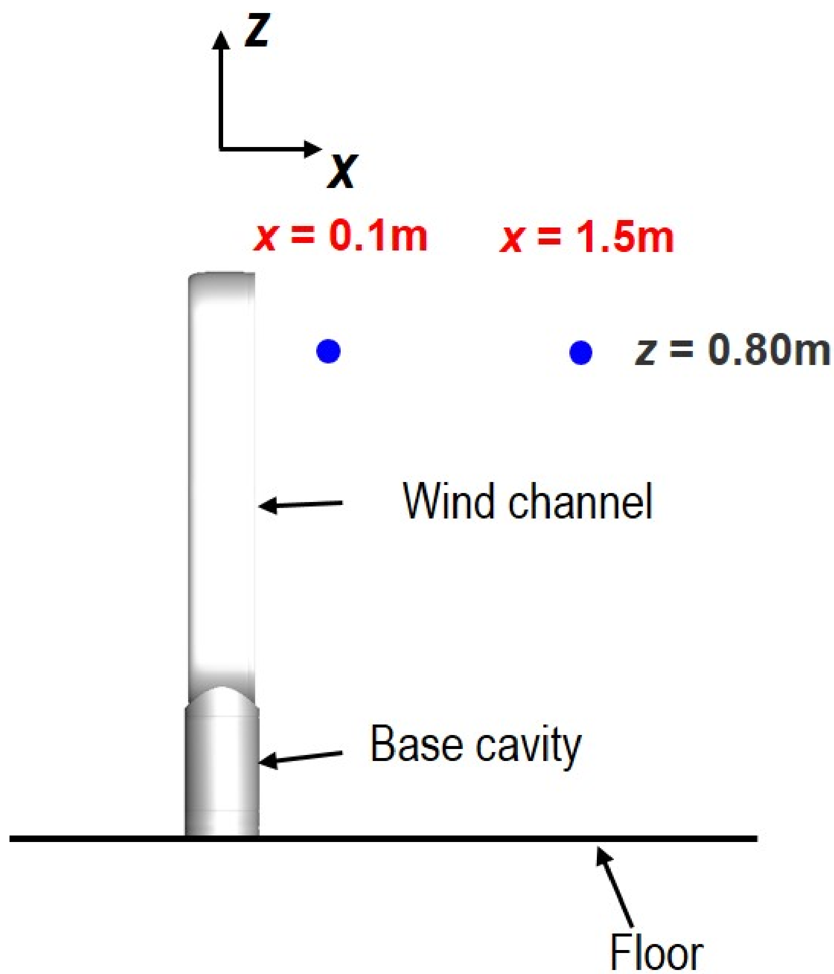

Figure 5.1. The definition of the noise sources and the receivers

5.1.2 Directivity Analysis

To further analyze on the noise around the bladeless fan, the sound pressure level at the front, back, right and left sides are calculated, and the locations of the receivers at the four sides are illustrated in Fig. 5.3(a).

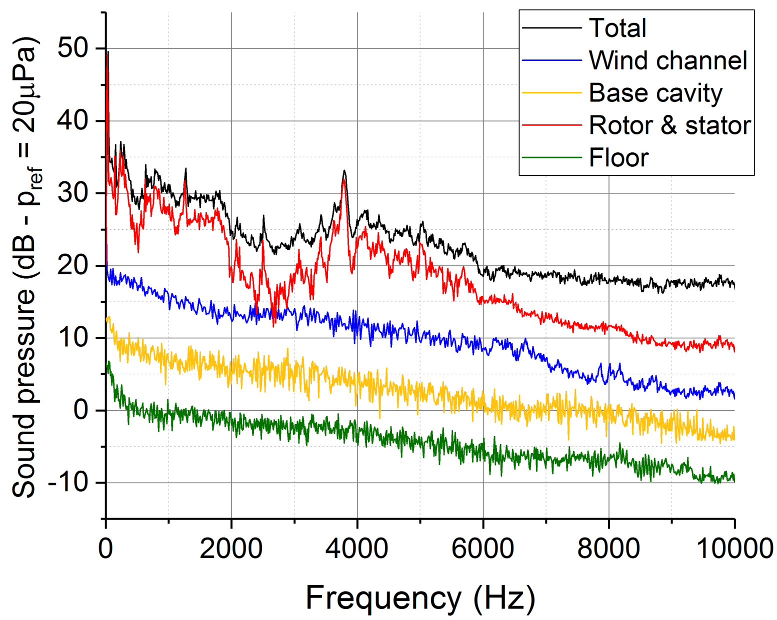

(a)

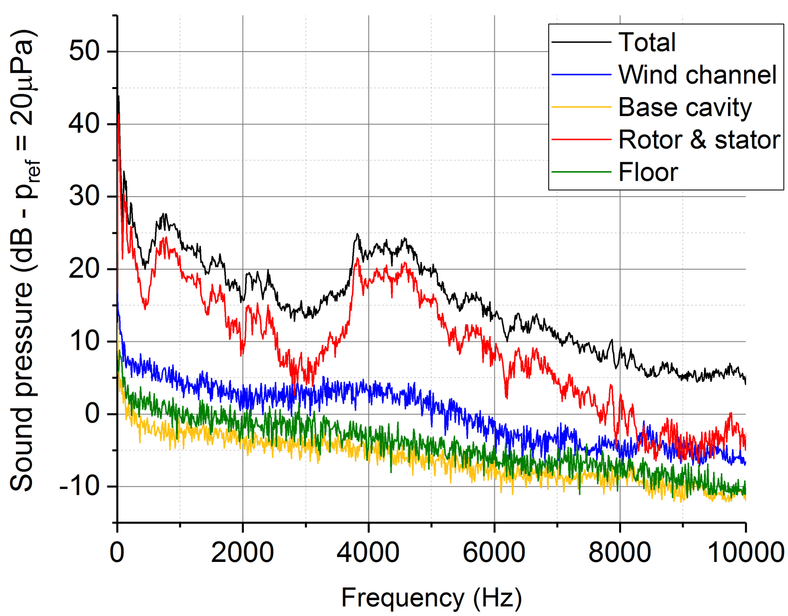

(b)

Figure 5.2. Contribution to sound pressure level by different parts (a) at near field, (b) at far field.

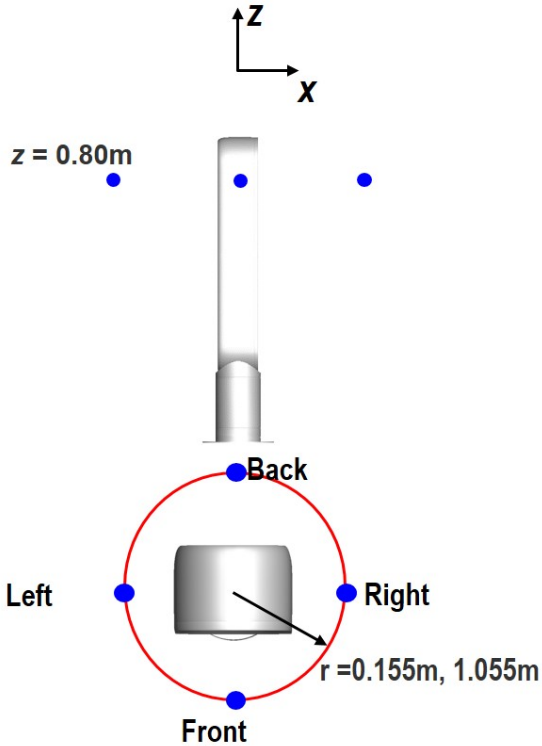

(a)

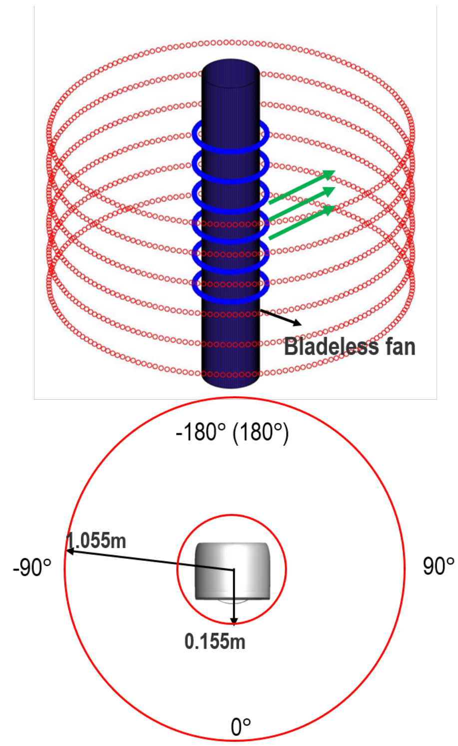

(b)

Figure 5.3. (a) Receivers on the front, back, right and left sides of the bladeless fan. (b) Receivers along circumferential direction

The sound pressure level on these four sides is shown in Fig. 5.4. At near field, the generated noise at the front and the back are larger than that at left and right, and the noise at the front is largest, as illustrated in Fig. 5.4(a). At the front side of the bladeless fan, the air blown out from the slit of the wind channel results in a large flow fluctuation and forms a turbulent mixing layer at the center plane of the bladeless fan. Thus the large pressure fluctuation causes a louder noise. At the back of the wind channel, the entrained air is relatively steady compared to that at the front, so the noise at the back is lower. At the left and right of the wind channel, the flow is more steady, so the noise level at the side is lowest. The sound pressure level at far field is presented in Fig. 5.4(b). The noise generated at the front is largest and the difference of sound pressure level between the front and other three sides is approximately 10dB. At far field, the receiver at the front is located at the influence region where the pressure fluctuation is large. Therefore, the noise level at the front is much larger than the other three sides.

For the present case, the rotating speed of the rotor is 8480rpm and the number of the blades on the rotor is 9, so the corresponding blade passage frequency is 1270Hz. In Fig. 5.4(a), a signature peak can be identified at around 1300Hz. Therefore, the blade passage frequency can be predicted accurately by the current simulation method.

To analyze the noise directivity of the bladeless fan further, receivers are also set up along the circumferential direction. Six height levels, z = 0.3m, 0.4m, 0.5m, 0.6m, 0.7m and 0.8m, are selected. In addition, two radial distances are chosen. The receivers located at r = 0.155m are used to analyze the noise at near field, while those located at r = 1.055m are for far field. On each height and radial distance, the azimuthal resolution of the receivers is 2°. The schematic of the receivers is shown in Fig. 5.3(b). To aviod the confusion in the figure, only receivers on three heights, z = 0.3m, 0.5m, 0.7m and at eight circumferential locations, $\psi = 0°, 45°, 90°, 135°, 180°, 225°, 270°, 315°$, are illustrated.

The sound pressure level at each receiver is calculated. Figure 5.5 illustrates the sound pressure level at near field. At each height level, the signature hotspot appears near 1300Hz, which corresponds to the blade passage frequency. With the increase of the height, two separated hotspots around 4000Hz appear. The value of sound pressure level at these two hotspots increases as the height increases. z = 0.3m corresponds to the bottom of the wind channel, the flow near the wind channel is a single jet. As the height increases, the flow divides into two separated jets. Thus, we can believe the two hotspots in sound pressure level contours correspond to the jets. The louder noise around 4000Hz may be caused by the turbulent jet at the near field.

Figure 5.6 shows the sound pressure level contours at r = 1.055m. At far field, the peak at blade passage frequency cannot be identified. With the increase of height, the sound pressure level increases. Since the influence zone at far field is at approximately $z = 0.7$m to $z = 0.8$m, the generated noise in this region is larger.

5.2 Influence of the Geometric Parameters of the Wind Channel

Similar to the investigations on aerodynamic performance, the influence of four parameters, the slit width, the height of the cross-section, the slit location and the profile of the cross-section is investigated.

As shown in Fig. 5.7, the pattern of sound pressure level for different designs of the wind channel are similar. Figure 5.7(a) shows the sound pressure level of different slit width. It is illustrated that with the decrease of the slit width, the noise generated by the fan increases. It matches with the changing tendency of x velocity. Figure 5.7(b) shows the sound pressure level obtained by the wind channel with different cross-sectional height. It is reported that the worst design exists. The wind channel with cross-sectional height of $H/c = 33.3\%$ generates the highest noise level. The effect of the slit location is presented in Fig. 5.7(c). It is indicated that the generated noise increases with increased x_0/c. It means as the slit moves to the trailing edge, the noise level produced by the wind channel becomes higher. The influence of the cross-sectional profile is shown in Fig. 5.7(d). The sound pressure levels obtained by the wind channel with different cross-sectional profiles are almost identical, which implies the profile of wind channel's cross-section has little impact on the aeroacoustic performance.

5.3 Summary

In this chapter, aeroacoustic performance of the bladeless fan is predicted by solving Navier-Stokes equations and Ffcows-Williams and Hawkings equation. Noise source analysis and noise directional analysis are conducted. In addition, the influence of the wind channel's geometric parameters is investigated. Main discoveries include: i) The rotor and stator inside the base are the predominated source of the noise generated by the bladeless fan. The wind channel is the secondary source.

ii) At near field, the produced noise at the front and the back of the bladeless fan are louder than those at left and right; at far field, the noise at the front is much larger than the other three sides.

iii) At near field, the peak at the blade passage frequency is predicted accurately. Another peak is obtained around 4000Hz.

iv) With the increase of the height, two separated jets appear over 4000Hz and the sound pressure level at these two hotspots increase.

v) At far field, the noise distribution at different heights are similar. The peak at blade passage frequency cannot be predicted, but the peak near 4000Hz is still able to be estimated.

vi) The noise generated by the bladeless fan is very sensitive to the geometric details of the wind channel. With the decrease of the slit or as the slit moves to the trailing edge, the noise increase significantly; The wind channel with the cross-sectional height of 4cm generates the loudest sound; Noise generated by the wind channel with different profiles of the cross-section are very similar.

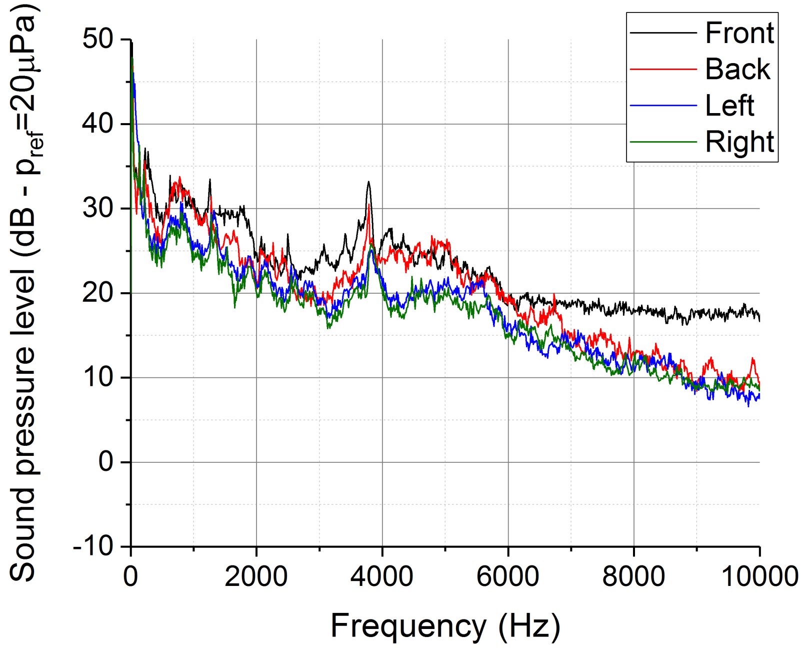

(a)

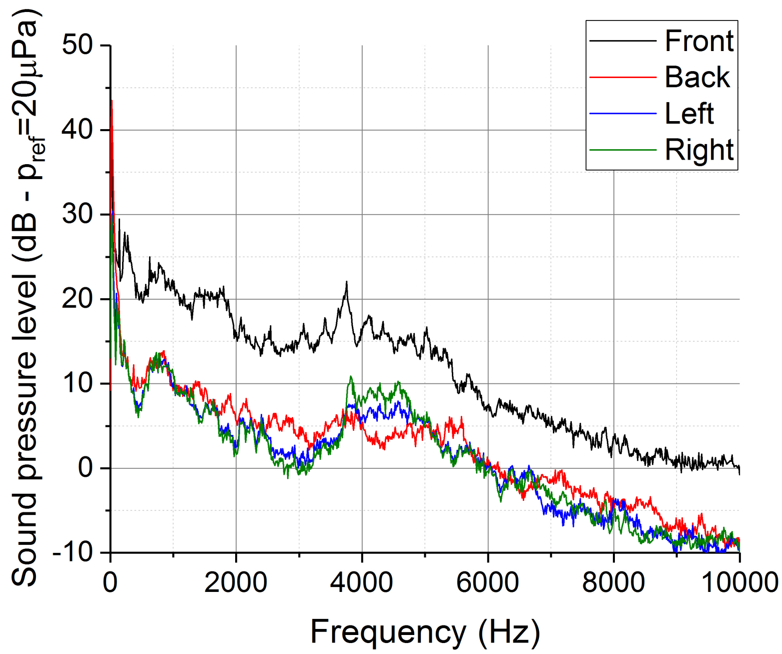

(b)

Figure 5.4. (a) Sound pressure level on four sides at near field. (b) Sound pressure level on four sides at far field.

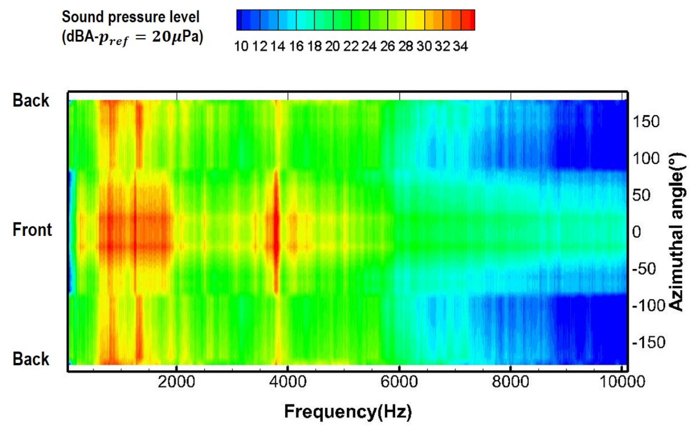
Sound pressure level
(dBA-$p_{ref} = 20\mu$Pa)
10 12 14 16 18 20 22 24 26 28 30 32 34
Back
Front
Back
2000
4000
6000
8000
10000
Frequency(Hz)
150
100
50
0
-50
-100
-150
Azimuthal angle(°)

(a)

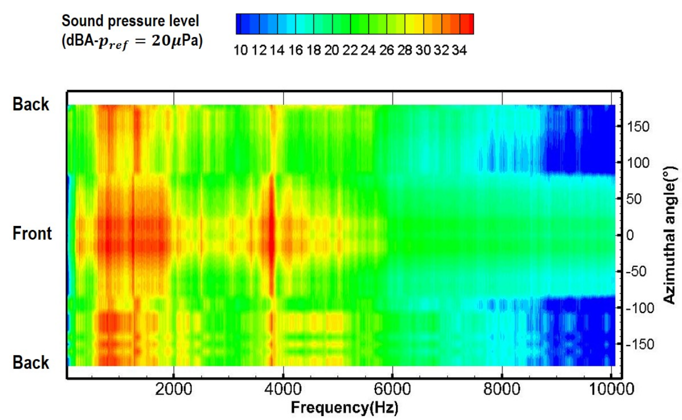
Sound pressure level
(dBA-$p_{ref} = 20\mu$Pa)
10 12 14 16 18 20 22 24 26 28 30 32 34
Back
Front
Back
2000
4000
6000
8000
10000
Frequency(Hz)
150
100
50
0
-50
-100
-150
Azimuthal angle(°)

(b)

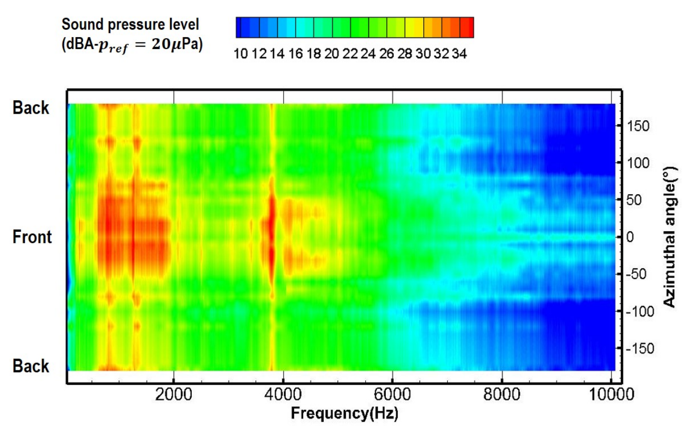
Sound pressure level
(dBA-$p_{ref} = 20\mu$Pa)
10 12 14 16 18 20 22 24 26 28 30 32 34
Back
Front
Back
2000
4000
6000
8000
10000
Frequency(Hz)
150
100
50
0
-50
-100
-150
Azimuthal angle(°)

(c)

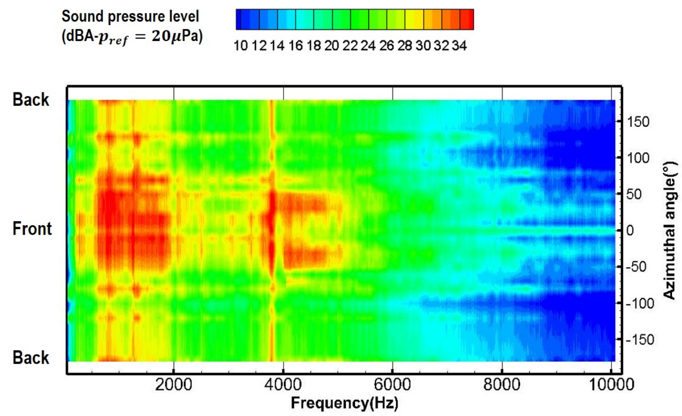

(d)

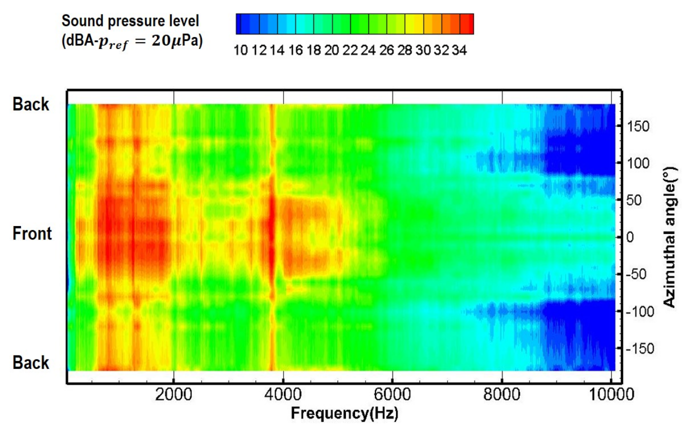

(e)

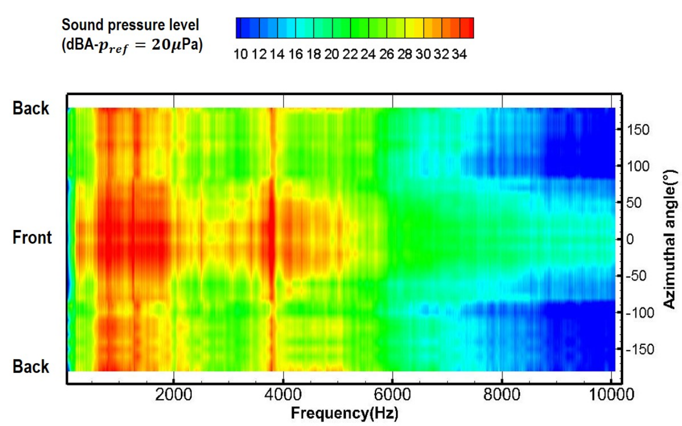

(f)

Figure 5.5. Sound pressure level contour (a) at $r = 0.155$m, $z = 0.3$m, (b) at $r = 0.155$m, $z = 0.4$m, (c) at $r = 0.155$m, $z = 0.5$m, (d) at $r = 0.155$m, $z = 0.6$m, (e) at $r = 0.155$m, $z = 0.7$m, (f) at $r = 0.155$m, $z = 0.8$m.

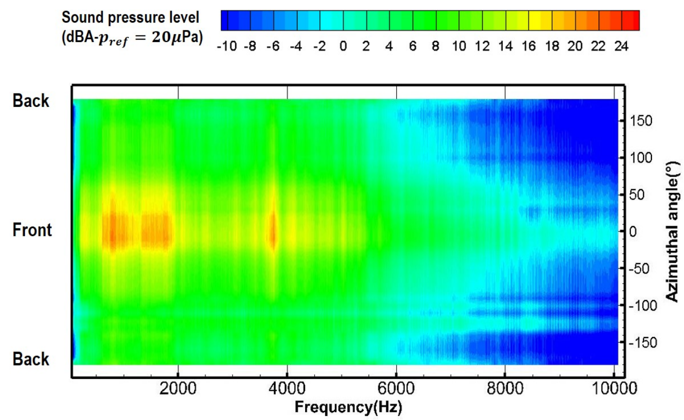
Sound pressure level
(dBA-$p_{ref} = 20\mu$Pa)
-10 -8 -6 -4 -2 0 2 4 6 8 10 12 14 16 18 20 22 24
Back
Front
Back
150
100
50
0
-50
-100
-150
Azimuthal angle(°)
2000
4000
6000
8000
10000
Frequency(Hz)

(a)

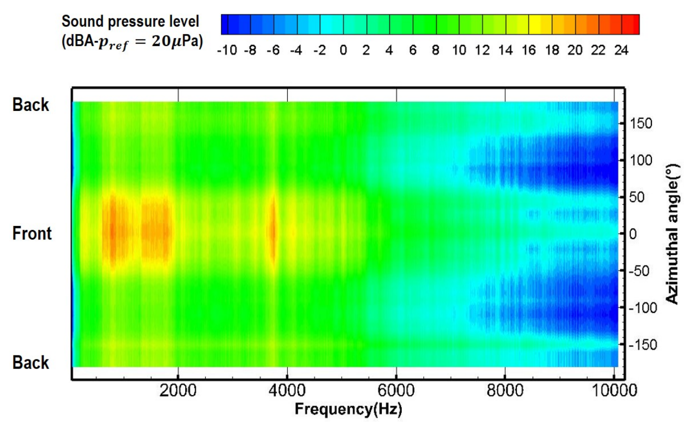
Sound pressure level
(dBA-$p_{ref} = 20\mu$Pa)
-10 -8 -6 -4 -2 0 2 4 6 8 10 12 14 16 18 20 22 24
Back
Front
Back
150
100
50
0
-50
-100
-150
Azimuthal angle(°)
2000
4000
6000
8000
10000
Frequency(Hz)

(b)

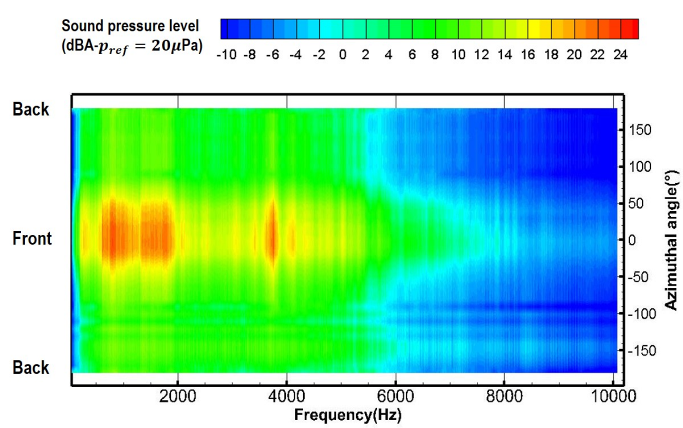
Sound pressure level
(dBA-$p_{ref} = 20\mu$Pa)
-10 -8 -6 -4 -2 0 2 4 6 8 10 12 14 16 18 20 22 24
Back
Front
Back
150
100
50
0
-50
-100
-150
Azimuthal angle(°)
2000
4000
6000
8000
10000
Frequency(Hz)

(c)

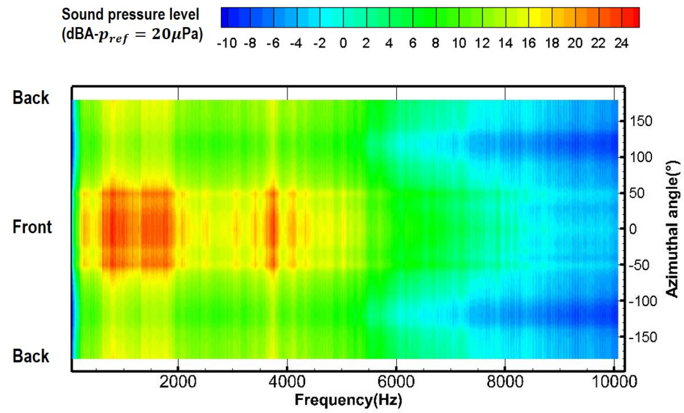

(d)

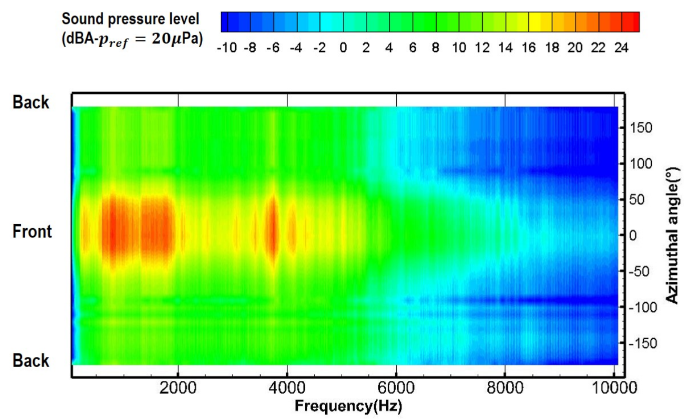

(e)

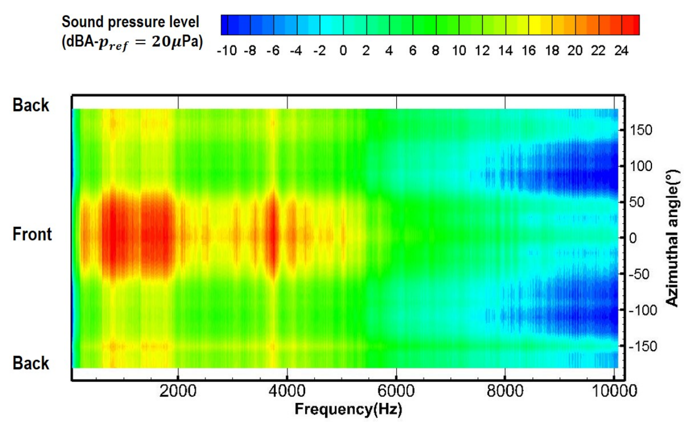

(f)

Figure 5.6. Sound pressure level contour (a) at $r = 1.055$m, $z = 0.3$m, (b) at $r = 1.055$m, $z = 0.4$m, (c) at $r = 1.055$m, $z = 0.5$m, (d) at $r = 1.055$m, $z = 0.6$m, (e) at $r = 1.055$m, $z = 0.7$m, (f) at $r = 1.055$m, $z = 0.8$m.

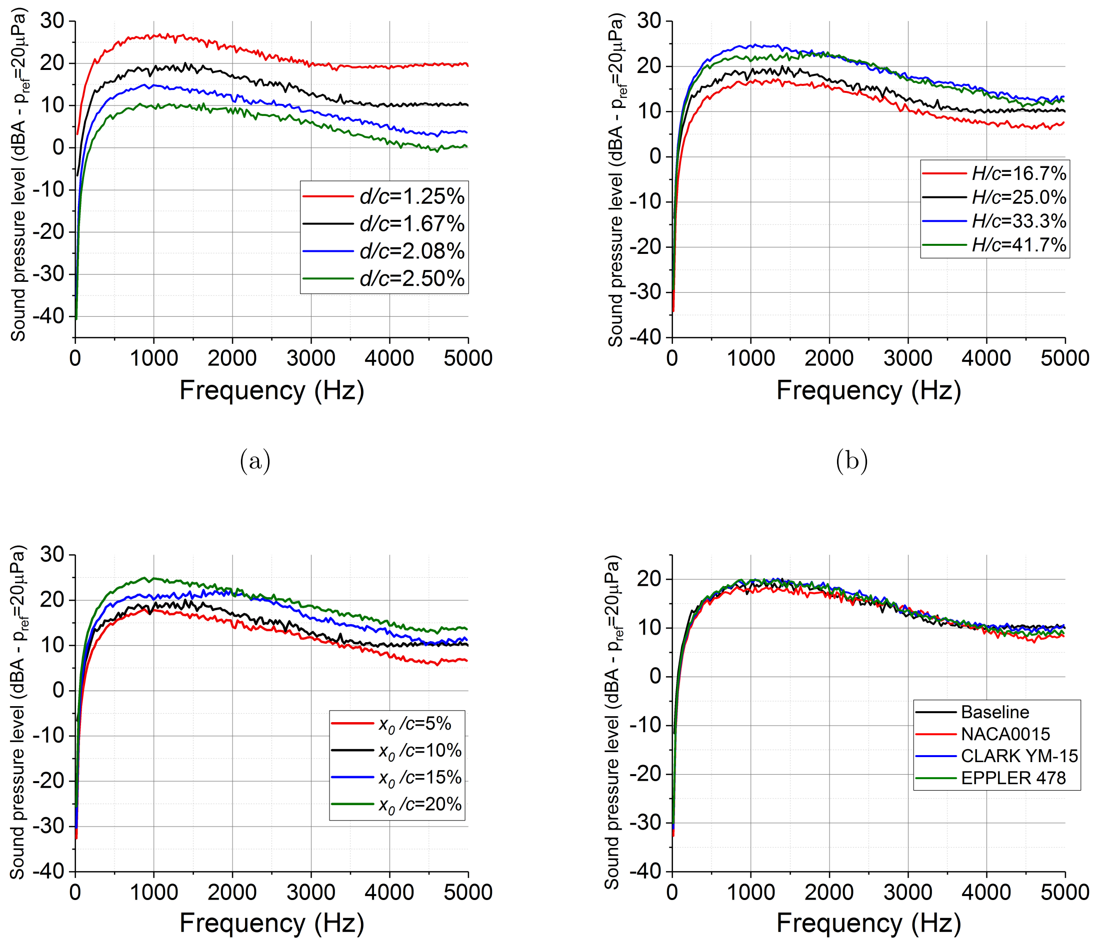

(a) (b)

(c) (d)

Figure 5.7. Sound pressure level (a) for different width of slit, (b) for different height of cross-section, (c) for different locations of slit, (d) for different profiles of cross-section.

6. Conclusions

The main purpose of the present study is to characterize the aerodynamic and aeroacoustic performances of the bladeless fan. Also, the effect of the wind channel's geometric parameters on the performances is investigated. Reynolds-Averaged Navier-Stokes approach and Large Eddy Simulation are employed to compute flow field inside and outside the bladeless fan; Ffowcs Willams and Hawkings model is used to predict noise generated by the bladeless fan.

When characterizing the aerodynamic and aeroacoustic performances of the bladeless fan, the entire fan prototype, including wind channel, base, rotor and stator, is adopted. When investigating the influence of the wind channel's geometric parameters, only wind channel is considered in simulations. Velocity contour, velocity profile, streamlines and ratio of mass flow rate are used to evaluate aerodynamic performance of the bladeless fan; Sound pressure level is used to evaluate aeroacoustic performance. The major discoveries include:

i) The flow outside the bladeless fan consists of the air blown out from the wind channel and the one entrained from the back and side of the fan. The air entrained from the side is the main source of the flow rate increase. As the air goes away from the fan, it moves upwards simultaneously.

ii) With the increase of the height, the wind outside the fan becomes less powerful, but the region of the influence zone becomes larger.

iii) From the horizontal view, the flow near the bladeless fan is formed by two separated jets. As far away from the fan, the two jets merge to a single jet.

iv) From the vertical view, at near field, two jets are located near the slit. As the distance away from the fan increases, the two jets merge to a single one. At the far field, there is a low energy region at the lower height.

v) The rotor and stator inside the base are the predominant source of the aerodynamic noise generated by the bladeless fan. The wind channel is the secondary source.

vi) At near field, the produced noise at the front and the back of the bladeless fan are louder than those at left and right; at far field, the noise at the front is much larger than the other three sides.

vii) With the increase of the height, two separated peaks appear over 4000Hz and the sound pressure level at these two hotspots increase, which is caused by the turbulent jet at near field.

viii) With the decrease of the slit width, both x velocity and the ratio of the mass flow rate increase. However, the generated noise level increases at the same time.

ix) The bladeless fan with the height of cross-section of 4cm has optimal aerodynamic performance. Also, it generated the highest noise level.

x) As the slit moves closer to the location of the maximum airfoil thickness, aerodynamic performance of the bladeless fan is improved and the generated noise level increases.

x) The wind channel with the cross-sectional profile of Eppler 478 has the best aerodynamic performance. Aeroacoustic performances of the fan with different cross-sectional profile are similar. Comparing to other geometric parameters, the profile of cross-section has little influence on performances of the bladeless fan.

In the present study, the aerodynamic and aeroacoustic performances of a bladeless fan prototype are characterized, and the influence of the geometric parameters of the wind channel is investigated. The results will be used to optimize the design of Midea new generation bladeless fan.

In the present study, the wind strength is the only criteria to evaluate the aerodynamic performance of the bladeless fan. However, in reality, the uniformity and steadiness of the wind may affect the comfort level experienced by the users. Thus, a general criterion needs to be come up with to evaluate the aerodynamic performance. According to the conclusions above, the noise level always increases with the increase of the wind strength, so when designing a bladeless fan, a compromise between aerodynamic performance and noise generation needs to be considered.

When investigating the influence of the wind channel's geometric parameters on the performances, the base, the rotor and stator are not considered. In future work, the entire fan prototype should be adopted to study the effect of the geometric parameters. Furthermore, more geometric parameters should be studied, such as the outlet angle and the aspect ratio of the wind channel.

REFERENCES

REFERENCES

Boddy, S. (2001). Cooling your home with fans and ventilation. Technical report, National Renewable Energy Lab., Golden, CO (US).

Brentner, K. S. and Farassat, F. (2003). Modeling aerodynamically generated sound of helicopter rotors. *Progress in Aerospace Sciences*, 39(2-3):83–120.

Bruegmann, R. (1978). Central heating and forced ventilation: origins and effects on architectural design. *Journal of the Society of Architectural Historians*, 37(3):143–160.

Cann, P. L. and Duell, R. J. (1972). Centrifugal fan. US Patent 3,698,833.

Canuto, V. and Cheng, Y. (1997). Determination of the smagorinsky–lilly constant cs. *Physics of Fluids*, 9(5):1368–1378.

Corsini, A., Delibra, G., and Sheard, A. G. (2013). A critical review of computational methods and their application in industrial fan design. *ISRN Mechanical Engineering*, 2013.

Cory, W. (2010). *Fans and ventilation: a practical guide*. Elsevier.

Crighton, D. (1975). Basic principles of aerodynamic noise generation. *Progress in Aerospace Sciences*, 16(1):31–96.

Crighton, D. G., Dowling, A. P., Ffowcs-Williams, J., Heckl, M., Leppington, F., and Bartram, J. F. (1992). Modern methods in analytical acoustics lecture notes.

Curle, N. (1955). The influence of solid boundaries upon aerodynamic sound. *Proceedings of the Royal Society of London. Series A. Mathematical and Physical Sciences*, 231(1187):505–514.

DOE, U. (2003). Improving fan system performance: A sourcebook for industry. prepared by lawrence berkeley national laboratory and resource dynamics corporation, washington. Technical report, DC DOE/GO-102003-1294./http://www1. eere. energy. gov/industry/bestpractices .

Farassat, F. (2007). Derivation of formulations 1 and 1a of farassat - nasa/tm-2007-214853. Technical report.

Ferziger, J. H. and Peric, M. (2012). *Computational methods for fluid dynamics*. Springer Science & Business Media.

Ffowcs Williams, J. E. and Hawkings, D. L. (1969). Sound generation by turbulence and surfaces in arbitrary motion. *Philosophical Transactions of the Royal Society of London. Series A, Mathematical and Physical Sciences*, 264(1151):321–342.

Fitton, N. G., Nicolas, F., and Gammack, P. D. (2011). Fan. US Patent 7,931,449.

Fluent, A. (2011). Ansys fluent theory guide. *ANSYS Inc., USA*, 15317:724–746.

Gammack, P. D., Nicolas, F., and Simmonds, K. J. (2012). Fan. US Patent 8,308,445.

Howe, M. (2002). Noise generated by a coanda wall jet circulation control device. *Journal of Sound and Vibration*, 249(4):679–700.

Hu, B.-b., OuYang, H., Wu, Y.-d., Jin, G.-y., Qiang, X.-q., and Du, Z.-h. (2013). Numerical prediction of the interaction noise radiated from an axial fan. *Applied acoustics*, 74(4):544–552.

Issa, R. I. (1986). Solution of the implicitly discretised fluid flow equations by operator-splitting. *Journal of computational physics*, 62(1):40–65.

Jafari, M., Afshin, H., Farhanieh, B., and Bozorgasareh, H. (2015). Numerical aerodynamic evaluation and noise investigation of a bladeless fan. *Journal of Applied Fluid Mechanics*, 8(1):133–142.

Jafari, M., Afshin, H., Farhanieh, B., and Sojoudi, A. (2016). Numerical investigation of geometric parameter effects on the aerodynamic performance of a bladeless fan. *Alexandria Engineering Journal*, 55(1):223–233.

Jafari, M., Sojoudi, A., and Hafezisefat, P. (2017). Numerical study of aeroacoustic sound on performance of bladeless fan. *Chinese Journal of Mechanical Engineering*, 30(2):483–494.

Jiang, C.-l., Chen, J.-p., Chen, Z.-j., Tian, J., OuYang, H., and Du, Z.-h. (2007). Experimental and numerical study on aeroacoustic sound of axial flow fan in room air conditioner. *Applied acoustics*, 68(4):458–472.

Kind, R. and Tobin, M. (1989). Flow in a centrifugal fan of the squirrel cage type. In *ASME 1989 International Gas Turbine and Aeroengine Congress and Exposition*, pages V001T01A025–V001T01A025.

Kinsler, L. E., Frey, A. R., Coppens, A. B., and Sanders, J. V. (1999). Fundamentals of acoustics. *Fundamentals of Acoustics, 4th Edition, by Lawrence E. Kinsler, Austin R. Frey, Alan B. Coppens, James V. Sanders, pp. 560. ISBN 0-471-84789-5. Wiley-VCH, December 1999.*, page 560.

Li, G., Hu, Y., Jin, Y., Setoguchi, T., and Kim, H. D. (2014). Influence of coanda surface curvature on performance of bladeless fan. *Journal of Thermal Science*, 23(5):422–431.

Li, H., Jin, X.-h., Deng, H.-s., and Lai, Y.-b. (2016). Experimental investigation on the outlet flow field structure and the influence of reynolds number on the outlet flow field for a bladeless fan. *Applied Thermal Engineering*, 100:972–978.

Lighthill, M. J. (1952). On sound generated aerodynamically i. general theory. *Proceedings of the Royal Society of London. Series A. Mathematical and Physical Sciences*, 211(1107):564–587.

Lilly, D. (1966). On the application of the eddy viscosity concept in the inertial sub-range of turbulence.

Liu, Y.-h., Hu, Q., and Xie, Y. (2010). Aerodynamic and acoustic predictions from chevron nozzles using fwh simulation. *Science Technology and Engineering*, 2010(35):24.

Meyer, C. and Kröger, D. (2001). Numerical simulation of the flow field in the vicinity of an axial flow fan. *International Journal for Numerical Methods in Fluids*, 36(8):947–969.

Mohamud, O. and Johnson, P. (2006). Broadband noise source models as aeroacoustic tools in designing low NVH HVAC ducts. In *SAE Technical Papers*.

Moukalled, F., Mangani, L., and Darwish, M. (2016). The finite volume method in computational fluid dynamics. *An advanced introduction with OpenFoam® and Matlab®. Nueva York: Springer.*

Patankar, S. V. and Spalding, D. B. (1983). A calculation procedure for heat, mass and momentum transfer in three-dimensional parabolic flows. In *Numerical Prediction of Flow, Heat Transfer, Turbulence and Combustion*, pages 54–73. Elsevier.

Powell, A. (1964). Theory of vortex sound. *The journal of the acoustical society of America*, 36(1):177–195.

Reese, H., Carolus, T., and Kato, C. (2007). Numerical prediction of the aeroacoustic sound sources in a low pressure axial fan with inflow distortion. *Fan noise*.

Sagaut, P. (2006). *Large eddy simulation for incompressible flows: an introduction*. Springer Science & Business Media.

Schmalz, J. and Kowalczyk, W. (2015). Implementation of acoustic analogies in openfoam for computation of sound fields. *Open Journal of Acoustics*, 5(02):29.

Smagorinsky, J. (1963). General circulation experiments with the primitive equations: I. the basic experiment. *Monthly Weather Review*, 91(3):99–164.

Theodorsen, T. (1948). *Theory of propellers*. McGraw-Hill publications in aeronautical science. McGraw-Hill Book Co., New York.

Wallis, R. A. (2014). *Axial Flow Fans: design and practice*. Academic Press.

Wetzel, D., Liu, F., Rosenberg, B., and Cattafesta, L. (2009). Acoustic characteristics of a circulation control airfoil. In *15th AIAA/CEAS Aeroacoustics Conference (30th AIAA Aeroacoustics Conference)*, page 3103.

Wilcox, D. C. (1998). *Turbulence modeling for CFD*, volume 2. DCW industries La Canada, CA.

Younsi, M., Bakir, F., Kouidri, S., and Rey, R. (2007). Numerical and experimental study of unsteady flow in a centrifugal fan. *Proceedings of the Institution of Mechanical Engineers, Part A: Journal of Power and Energy*, 221(7):1025–1036.

Zhang, P., Yan, B., and Dai, C. (2012). Lift enhancement method by synthetic jet circulation control. *Science China Technological Sciences*, 55(9):2585–2592.